ABSTRACT

Title of thesis: MORPHOTROPIC PHASE BOUNDARY
                    ENGINEERING IN FERROELECTRICS

                    Yueying Liu, Master of Science, 2013

Thesis Directed By: Professor Manfred Wuttig
                       Department of Materials Science and
                       Engineering

Barium calcium titanate (BCT), Sr-doped BCT (BSCT), and barium strontium calcium titanate-barium zirconate titanate xBSCT-(1-x)BZT (0.1≤x≤0.55) ceramics have been prepared by sol-gel method and solid state sintering process. The temperature dependences of dielectric constant and loss at different frequencies for all compositions were characterized and analyzed. For xBSCT-(1-x)BZT ceramics with 20% Ba in BCT substituted by Sr, the paraelectric-to-ferroelectric (cubic-to-tetragonal/rhombohedral) phase transition temperature T_C increases for compositions of x<0.28, stays almost unchanged for x=0.28, and reduces significantly for x>0.28 with respect to the undoped xBCT-(1-x)BZT. Compared with BCT-BZT system, Sr-doped BSCT-BZT system shows a triple point at lower composition and temperature, and a morphotropic phase boundary (MPB) which is less vertical with respect to the composition axis in the phase diagram. Our results demonstrate that doping is an effective way to engineer MPB of BCT-BZT system and thus can help develop more compositions suitable for applications requiring large piezoelectric coefficient.

MORPHOTROPIC PHASE BOUNDARY ENGINEERING IN
FERROELECTRICS

By

Yueying Liu

Thesis submitted to the Faculty of the Graduate School of the
University of Maryland, College Park, in partial fulfillment
of the requirements for the degree of
Master of Science
2013

Advisory Committee:
Professor Manfred Wuttig, Chair
Professor Lourdes Salamanca-Riba
Associate Professor Isabel Lloyd
Professor James Cullen

Dedication

To my grandmother

Acknowledgements

I have received a lot of generous helps and supports from many people during my graduate study. Without them, the completion of this thesis would not have been possible. I own my deepest gratitude to all of these great people.

First of all, I would like to thank my advisor Professor Manfred Wuttig for his full support and invaluable guidance during the past five years. He has always been there offering his help whenever I encountered a problem. I will never forget the meetings and discussions I have enjoyed with him about research and life. His vast knowledge and passion for science are indeed admirable, for which I would like to show my sincerest respect.

I am extremely grateful to Dr. Isabel Lloyd who has generously allowed me to use her lab for preparing all my samples. I would also like to give my thanks to all my colleagues and friends, Dr. Shenqiang Ren, Dr. Yemei Han, Dr. Richard Bergstrom, and Tong Ren. They have been so kind to be willing to spend time teaching me how to prepare samples or showing me how to operate some characterizing apparatus whenever I came to them for help.

I would like to express my special thanks to all the members of my family. At every moment of my life, my parents and my sister have always been there giving me their unconditional love and unwavering support wherever I am and whatever I do. Without them standing beside me, I would never have gone so far to where I am now. Thank you and love you so much! Finally, I want to thank my beloved Ying, who has accompanied me spending every happy and difficult moment during the past ten years. I couldn't imagine how I would have come to

this point without your love and support. I wish, am looking forward to, and also

believe that we will have the most amazing life together in the rest of our lifetime.

Table of contents

List of Tables

List of Figures

Chapter 1 Introduction

1.1 Morphotropic Phase Boundary (MPB)

MPB is the boundary in a temperature-composition phase diagram, separating two low-temperature phases with different crystallographic symmetries (typically rhombohedral and tetragonal), as shown in Fig.1.1 [1, 2]. The phase transition across MPB can happen by variation of either temperature or composition. The investigation on MPB has been carried out mostly in ferroelectric lead-based perovskite oxide solid solutions ($PbZrO_3$-$PbTiO_3$ (PZT), $Pb(Mg_{1/3}Nb_{2/3})O_3$ (PMN)-$PbTiO_3$ (PT) and $Pb(Zn_{1/3}Nb_{2/3})O_3$ (PZN)-PT), of which PZT solid solution was the first and most widely studied system [3-8]. As seen from the phase diagram of ferroelectric PZT with MPB marked in Fig.1.1, there are totally three MPB-related different structures in the temperature and composition range covered in the phase diagram. In the high temperature solid state region, PZT forms a complete solid solution corresponding to the paraelectric cubic phase. In the low temperature solid state region, there are two different phases separated by MPB, the ferroelectric rhombohedral phase (space group: R3m) near $PbZrO_3$ side and the ferroelectric tetragonal phase (space group: P4mm) near $PbTiO_3$ side.
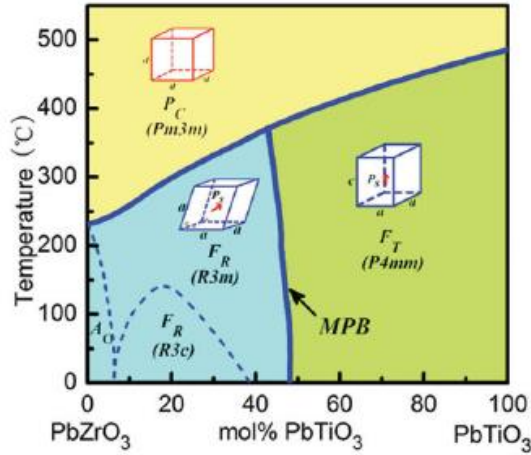
Fig. 1.1 Temperature-composition phase diagram of ferroelectric PZT system [1] modified based on the phase diagram given in [2].

MPB can only exist in a binary/pseudobinary phase diagram where two end compositions have different low crystallographic symmetries below some critical temperatures (T_C), above which a complete solid solution region with higher symmetry is formed. Therefore，in binary alloy systems like Cu-Ni, no MPB can form in the phase diagram (in Fig. 1.2) because there is no structural phase transition happening in the solid solution region with the two end compositions Cu and Ni always showing the same crystallographic symmetry FCC. Because the temperature of the phase transition through MPB ($T_{MPB} < 350^{\circ}C$ in PZT) is usually far lower than the melting temperature ($T_M > 1300^{\circ}C$ in PZT [9]), diffusion will be too slow to accommodate the stress induced during the phase transition due to the different crystallographic symmetries between the parent phase and the product phase. Therefore, it is believed that a special diffusionless transformation takes place at MPB, during which only displacive atomic arrangement occurs without compositional change involved [10].

2
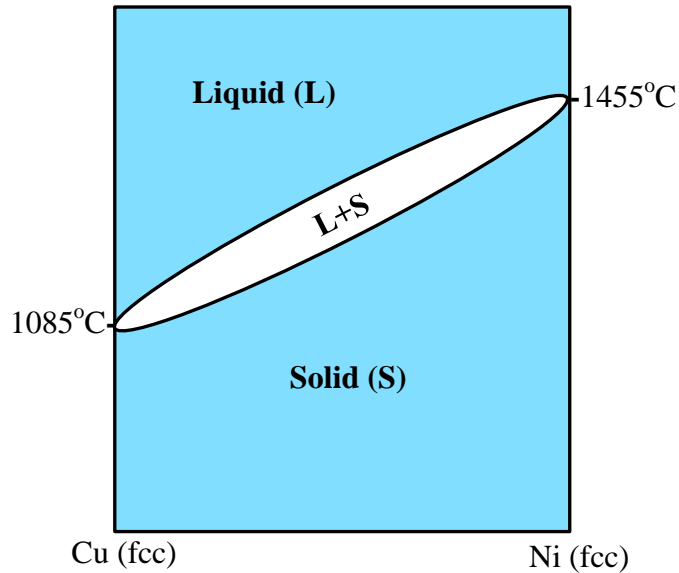
Fig. 1.2 Schematic binary phase diagram of Cu-Ni alloy.

1.2 Structural study on MPB in lead-based ferroelectrics

A large volume of work has been devoted to determining the structural state of ferroelectric solid solutions with compositions near MPB in order to illustrate the origin of the large piezoelectric response observed in these compositions [3]. The key progress which has been made is based on the discovery that in several ferroelectric solid solution systems with MPB including PZT, PMN-PT and PZN-PT, a monoclinic phase (space group: Cm/Pm) has formed in compositions near the MPB according to diffraction data obtained either by high resolution x-ray or neutron scattering technique [4, 5, 11-14]. The appearance of this monoclinic phase seems to be a universal feature connected to the high piezoelectric coefficient shown by compositions near MPB. However, the interpretation of this monoclinic phase and the resultant large piezoelectric coefficient has been remained controversial. There are several different structural models proposed to explain the monoclinic phase identified from diffraction

patterns and the origin of the large piezoelectric response at MPB [15], and the most popular two models give totally different interpretations and will be described next.

1.2.1 Real monoclinic phase model

The first model to be introduced was proposed by Noheda et al. [5, 7, 16]. According to Noheda's model, the monoclinic peak splitting observed in the diffraction pattern of PZT and other related ferroelectric solid solutions near MPB indeed comes from an existing monoclinic phase. This monoclinic phase has been induced by local monoclinic distortion which gives rise to long-range rhombohedral or tetragonal distortion and thus the coexistence of these two phases at MPB as detected by regular x-ray diffraction technique. Besides, Noheda's model points out the fact that this monoclinic phase belongs to space group Cm/Pm which is the subgroup of both rhombohedral R3m and tetragonal P4mm. This suggests that this monoclinic phase is an intermediate phase acting as a bridge connecting the rhombohedral and tetragonal phases on the opposite sides of MPB. Based on this structural model, the large piezoelectric response near MPB is considered to be a direct result of the low-symmetry monoclinic phase in which the polarization vector can be rotated in the plane between two pseudocubic directions: $[001]_{pc}$ (the polar axis of tetragonal phase) and $[111]_{pc}$ (the polar axis of rhombohedral phase).

1.2.2 Monoclinic adaptive phase model

The second structural model has been developed by Khachaturyan et al. [10, 17-19], which is usually called "adaptive phase" model and has proved to be

very successful by showing close agreement with experimental results. According to this adaptive phase model, the monoclinic symmetry indicated by diffraction pattern doesn't correspond to a really existing monoclinic phase, but is just a nanodomain-averaged result from a periodic lamellar structure composed of nanotwinned rhombohedral or tetragonal domains. The monoclinic phase is called adaptive phase, and the twin-related rhombohedral/tetragonal nanodomain state is called adaptive state which is inhomogeneous on the nanoscale, but can be seen as a homogeneous state on a larger scale. When x-ray or neutrons with large coherence length are used to detect the twin-related nanodomain structure, the domain-averaged structure with lower symmetry will be seen instead of the structure of the individual domain. In order to explain why the monoclinic adaptive phase has formed in these lead-based ferroelectrics at MPB and how the adaptive state is related to the large piezoelectric coefficient, we need to introduce the well-developed adaptive phase theory in martensites which has been reported by Khachaturyan et al. in his early work [20].

1.2.2.1 Adaptive phase theory in martensites

Martensitic phase transition is a diffusionless structural phase transition, in which the elastic energy generated by crystal-lattice mismatch between parent phase and product phase (martensite) with different crystallographic symmetries is about equal or much larger than the transformation chemical driving force. Due to the large lattice mismatch induced elastic energy, martensitic phase transition has to proceed along a path which can provide almost complete accommodation of the crystal-lattice mismatch. As a result, a special structured martensite is

formed, characterized by martensitic macroplates consisting of quasi-periodic alternated lamellar domains of two twin-related orientational variants of the martensite phase as shown in Fig. 1.3. The period λ of the lamellae is determined by a balance of the the elastic and twin boundary energies:

$$\lambda = \left(\frac{\Upsilon_{twin}}{\mu\epsilon_0^2}D\right)^{1/2}, \tag{1.1}$$

where D is the width of the macroplate, Υ_{twin} is the twin boundary/domain wall energy, and $\mu\epsilon_0^2$ is the lattice-mismatch induced elastic energy. Since λ is proportional to $\sqrt{\Upsilon_{twin}}$, miniaturization of twin-related lamellar domains can happen if Υ_{twin} becomes very small. When the size of the twin-related martensite domains is comparable to the interatomic distance, the crystal lattice parameters measured by conventional diffraction techniques will no longer be the lattice parameters of the normal martensite phase forming the miniaturized twin domains (microdomains), but the averaged lattice parameters over the microtwins. This microtwinned state of the martensite phase is called adaptive state and the corresponding domain-averaged phase is called adaptive martensite phase.
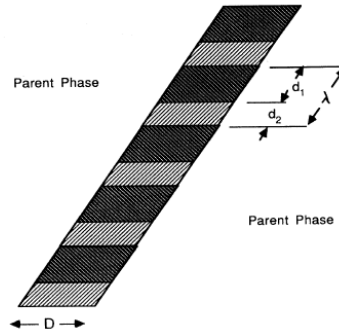
Fig. 1.3 Schematic representation of the martensitic phase plate composed of twin-related lamellae of two orientational variants of the martensitic phase [20].

6

The adaptive martensite phase has lower symmetry than the normal (non-twinned) martensite, and its lattice parameters are adaptive depending on the volume ratio of the two orientational variants forming the microtwinned lamellar domains.

In a cubic-to-tetragonal martensitic phase transition, a cubic-to-tetragonal crystal lattice rearrangement takes place to transform the parent cubic crystal lattice parameter a_c into tetragonal lattice parameters c_t and a_t. Such transformation can generate three orientational variants of the tetragonal phase, in which tetragonal axis is along the direction of $[100]_c$, $[010]_c$ and $[001]_c$ in the cubic lattice, respectively, as shown in Fig. 1.4a. The stress-free strain tensors for these three orientational variants can be written as Eq. (1.2):

$$\epsilon(1)^0_{ij} = \begin{bmatrix} \epsilon^0_{33} & 0 & 0 \\ 0 & \epsilon^0_{11} & 0 \\ 0 & 0 & \epsilon^0_{11} \end{bmatrix},$$

$$\epsilon(2)^0_{ij} = \begin{bmatrix} \epsilon^0_{11} & 0 & 0 \\ 0 & \epsilon^0_{33} & 0 \\ 0 & 0 & \epsilon^0_{11} \end{bmatrix},$$

$$\epsilon(3)^0_{ij} = \begin{bmatrix} \epsilon^0_{11} & 0 & 0 \\ 0 & \epsilon^0_{11} & 0 \\ 0 & 0 & \epsilon^0_{33} \end{bmatrix}, \qquad (1.2)$$

where the strain components, $\epsilon^0_{33} = \frac{c_t - a_c}{a_c}$ and $\epsilon^0_{11} = \frac{a_t - a_c}{a_c}$, measure the lattice mismatch between the tetragonal martensite phase and matrix parent cubic phase. If we consider a macroplate in adaptive martensite state composed of alternating twin-related microdomains of the two tetragonal orientational variants with the

first two strain tensors in Eq.(1.2), the total macroscopic shape change due to cubic-to-tetragonal transition can be calculated by the average of the respective strains:

$$\bar{\epsilon}_{ij} = \omega\epsilon(1)_{ij}^0 + (1-\omega)\epsilon(2)_{ij}^0$$

$$= \begin{bmatrix} \omega(\epsilon_{33}^0 - \epsilon_{11}^0) + \epsilon_{11}^0 & 0 & 0 \\ 0 & \omega(\epsilon_{11}^0 - \epsilon_{33}^0) + \epsilon_{33}^0 & 0 \\ 0 & 0 & \epsilon_{11}^0 \end{bmatrix} \quad (1.3)$$

where ω and 1-ω are the volume fractions of the two orientational variants.

In order to produce a stress-free boundary between the tetragonal phase and the cubic phase matrix, the mismatch tensor $\bar{\epsilon}_{ij}$ has to be an invariant plane strain, which means one of the three diagonal components, $\bar{\epsilon}_{11}$, $\bar{\epsilon}_{22}$ and $\bar{\epsilon}_{33}$, has to be zero. Since $\bar{\epsilon}_{33}(= \epsilon_{11}^0 = \frac{a_t - a_c}{a_c})$ can't be zero, it is only possible that $\bar{\epsilon}_{11}$ or $\bar{\epsilon}_{22}$ equals zero. The relations $\bar{\epsilon}_{11}=0$ and $\bar{\epsilon}_{22}=0$ correspond to two equivalent situations. With $\bar{\epsilon}_{11}=0$, we can obtain the value of $\omega = \omega_0 = \frac{\epsilon_{11}^0}{\epsilon_{11}^0 - \epsilon_{33}^0} > 0$. Substituting ω_0 into Eq. (1.3), we can obtain,

$$\bar{\epsilon}_{ij} = \begin{bmatrix} 0 & 0 & 0 \\ 0 & \epsilon_{33}^0 + \epsilon_{11}^0 & 0 \\ 0 & 0 & \epsilon_{11}^0 \end{bmatrix} \quad (1.4)$$

Applying Eq. (1.4) to cubic axes, $a_1=(a_c, 0, 0)$, $a_2=(0, a_c, 0)$, and $a_3=(0, 0, a_c)$, the lattice parameters of the adaptive martensite phase can be obtained as:

$$a_{ad} = a_c, \quad (1.5a)$$

$$b_{ad} = a_t + c_t - a_c, \quad (1.5b)$$

$$c_{ad} = a_t \qquad\qquad\qquad (1.5c)$$

The lattice parameters shown in Eq. (1.5) correspond to a completely stress-accommodating adaptive martensite. Eq. (1.5) is obtained with $\omega = \omega_0$ and is named special invariance condition which is only valid when there is no external field applied. If an external field exists, the volume fraction will change accordingly with one variant promoted and the other suppressed, and a large shape change can be induced as a result. The general lattice parameters of the adaptive phase with the arbitrary volume fraction of ω can be obtained based on the strain tensor shown in Eq. (1.3):

$$a_{ad} = a_t + (c_t - a_t)\omega \qquad\qquad\qquad (1.6a)$$

$$b_{ad} = c_t - (c_t - a_t)\omega \qquad\qquad\qquad (1.6b)$$

$$c_{ad} = a_t \qquad\qquad\qquad (1.6c)$$

From Eq. (1.6), a general invariance condition can be extracted, which is $a_{ad} + b_{ad} = a_t + c_t$ (obtained by adding Eq. (1.6a) and Eq. (1.6b)), and $c_{ad} = a_t$ (Eq. (1.6c)).

The special invariance and general invariance conditions tell us that there is an intrinsic relationship between the lattice parameters of the adaptive martensite phase, parent cubic phase and tetragonal martensite phase which can be readily checked in experimental data and thus works as a fingerprint of the existence of an adaptive phase.

With the strain tensors described in Eq. (1.3) and (1.4), the adaptive martensite phase appears to be an orthorhombic phase as long as the three

adaptive phase lattice axes are kept parallel to the three lattice vectors of the parent cubic phase lattice, which is not the case in real situation. One of the three angles between different pair of lattice vectors has actually been changed by a small amount differing from 90° as shown in Fig. 1.4b. When two orientational variants with tetragonal axis along $[100]_c$ and $[010]_c$ direction form a stress-accommodated macroplate consisting of alternating domains of the two orientational variants, the different variant domains are twin-related with the twin/domain boundary to be $(110)_c$ plane because there is no lattice mismatch between the two variants by sharing $(110)_c$ plane. As shown in Fig. 1.4b, rotation of the two orientational variants occurs with twinning happening at (110) plane in order to fill the gap produced between two orientational variants during cubic-to-tetragonal lattice rearrangement. Therefore, the symmetry of the resultant adaptive martensite phase consisting of twinned domains of the two tetragonal variants is monoclinic.

(a)

Variant 1   Variant 2   Variant 3

(b)
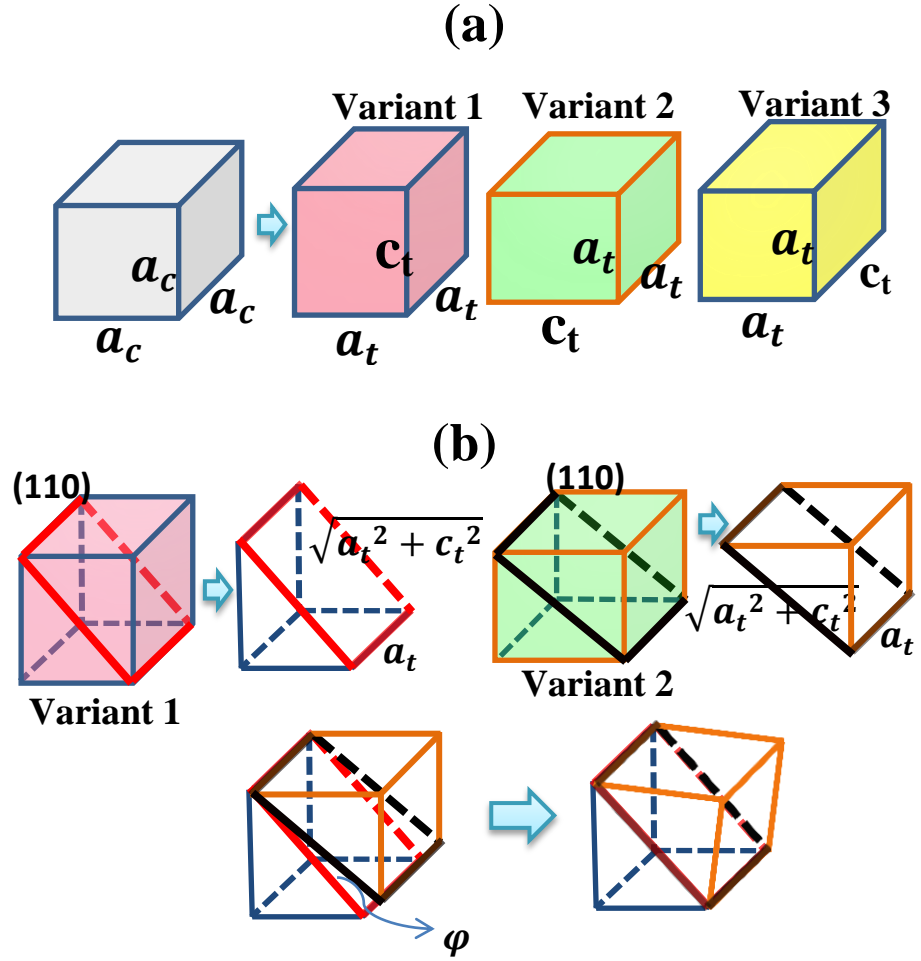
Fig. 1.4 (a) Cubic lattice and the three tetragonal orientation variants generated by lattice arrangement during cubic-to-tetragonal martensitic phase transition; (b) the twinning of variant 1 and 2 by sharing lattice matched (110) planes introduces rotation of the two variants caused by their coherent adjustment in order to fill the gap formed as a result of the cubic-to-tetragonal transformation.

The special invariance condition represented by Eq. (1.5) was experimentally checked and a good agreement was achieved between the lattice parameters of martensite adaptive phase predicted by Eq. (1.5) and the experimentally measured lattice parameters in Fe-Pd alloy, as displayed in Fig. 1.5 [20]. Fig. 1.6 indicates that as Eq. (1.5) predicted, the lattice parameter a_t and a_c continues into the intermediate martensite adaptive phase as a_{ad} and c_{ad},

respectively, while the lattice parameter b_{ad} calculated by $b_{ad} = a_t + c_t - a_c$

presents excellent agreement with the experimental points. Thus, the intermediate

phase is believed to be an adaptive martensite phase formed by microtwinned

tetragonal martensite phase.
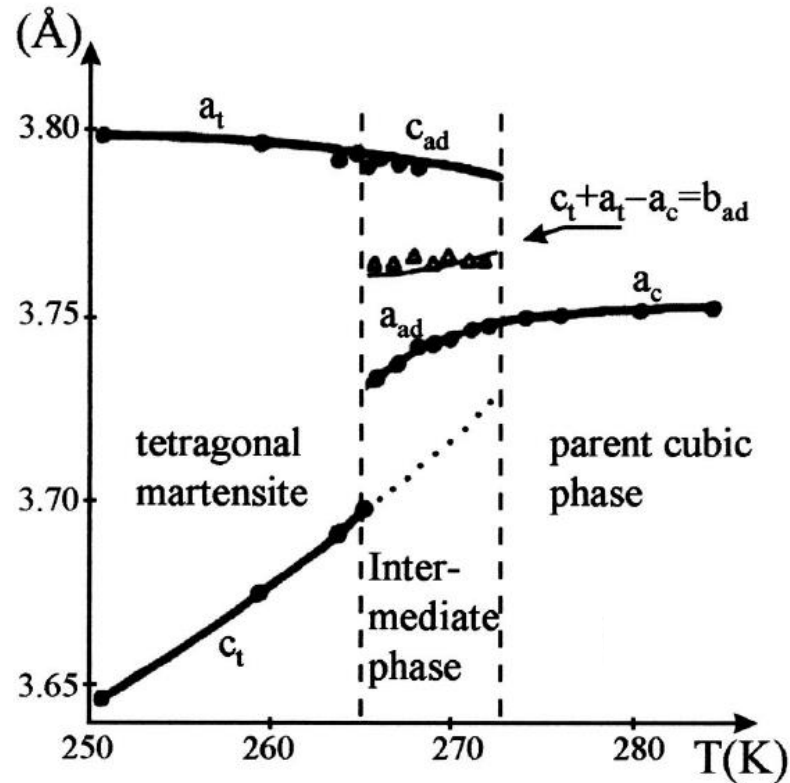
Fig. 1.5 Temperature dependence of lattice parameters of parent cubic phase, intermediate adaptive phase and tetragonal martensite phase in Fe-30.1 at. % Pd alloy. Dots and triangles correspond to experimental data points measured by Seto et. al. [21]. The dashed line is the extrapolated c_t. The thin line in the intermediate phase region is calculated by $b_{ad} = a_t + c_t - a_c$.

1.2.2.2 Extension of adaptive phase theory in phase transition through MPB in ferroelectrics

The phase transition at MPB in ferroelectric PZT, PMN-PT and PZN-PT

is similar to martensitic phase transition because they are both diffusionless

transitions in which a displacive lattice rearrangement occurs to complete the structural phase change. So, like in martensite phase transition, the formation of twin-related domain structure in martensites is also favored to accommodate the stress induced by the different symmetries of the two phases involved in the phase transition across MPB in ferroelectrics. However, MPB transition in ferroelectrics is different from the martensitic phase transition because electric polarization has to be added into consideration. The formation of twin-related domain structure will be affected by the requirement of both stress-accommodation and the minimization of depolarization energy. Nevertheless, since the polar anisotropy is drastically reduced or vanished at MPB (Fig. 1.6) which has been predicted by using the 2-4-6 free energy approximation of the Ginzburg-Landau-Devonshire theory [10], there is no extra domain energy produced in domain boundary due to the additional polarization term. Structural domains at MPB will just show martensite-like pattern as long as the distribution of polarization vectors in the structural domains can minimize the depolarization energy. Similar to martensite, a significant reduction in domain wall energy should also induce the minimization of domains in ferroelectrics which has been experimentally observed in PZT near MPB as shown in Fig. 1.7 [6, 22]. The formation of the twin-related nanodomains at MPB is believed to be the result of the drastically reduced or vanishing domain wall energy at MPB. The drastic reduction or vanishing of domain wall energy at MPB is attributed to the drastically reduced or vanishing polar anisotropy.
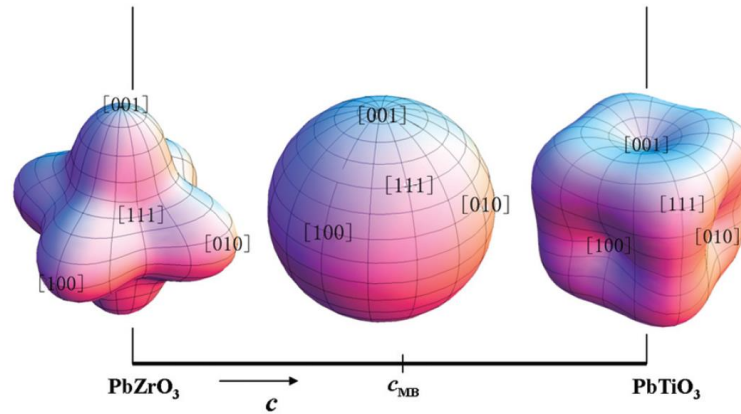
Fig. 1.6 Schematic illustration of polar anisotropy energy as function of the concentration of PT in PZT calculated based on the traditional 2-4-6 free energy approximation of the Ginzburg-Landau-Devonshire theory, indicating the polar axis for rhombohedral $PbZrO_3$ and tetragonal $PbTiO_3$ is <111> and <100>, respectively, while the $PbZrO_3$-$PbTiO_3$ alloy is polar isotropic at MPB [23].
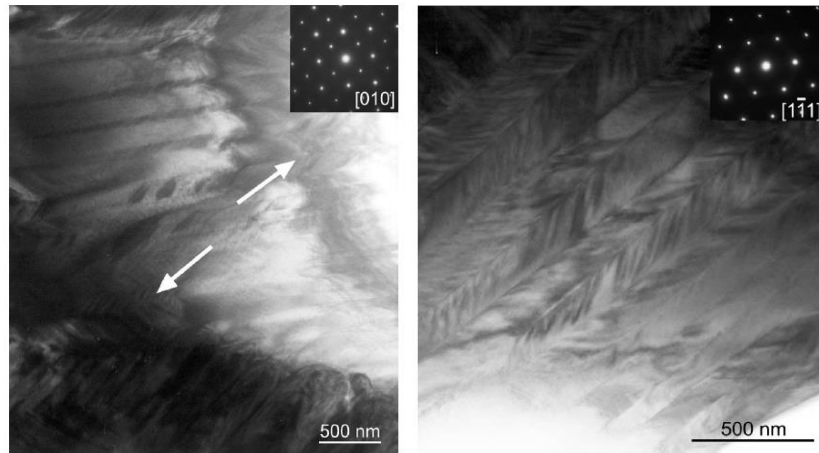
Fig. 1.7 Bright field TEM image of PZT at MPB with the Zr/Ti ratio of 52/48 (left) and 53/47 (right) showing the appearance of fine nanodomains marked with white arrows [6].

According to adaptive phase theory, adaptive martensite phase has monoclinic symmetry resulting from the averaged tetragonal microdomains, which can perfectly explain the monoclinic peak splitting of ferroelectrics with nanodomain structure near MPB. In order to support that the ferroelectric MPB

phase, showing nanodomain structure and monoclinic symmetry, is indeed an adaptive phase composed of tetragonal/rhombohedral nanodomains, another important evidence has to be identified, i.e. the intrinsic relationship between lattice parameters of the immediate adaptive phase and the two phases on the opposite sides of MPB.

The special invariance condition and general invariance condition have been checked in ferroelectric solid solutions with monoclinic phase near MPB and both of them have been confirmed. Fig. 1.8 gives the temperature dependence of lattice parameters for PMN-xPT [18]. From Fig. 1.8, it can be seen that a_t, the lattice parameter of tetragonal phase in intermediate temperature region and a_c, the lattice parameter of cubic phase in high temperature region are extended into the monoclinic region at low temperatures and become b_m (c_{ad} in Eq. (1.5c)) and a_m(a_{ad} in Eq. (1.5a)), respectively. According to the special invariance condition, the third lattice parameter c_m (b_{ad} in Eq. (5a)) should follow $c_m = a_t + c_t - a_c$, which can be adjusted to be $c_t = c_m - a_t + a_c = c_m - b_m + a_m$. Indeed, the predicted c_t in monoclinic region is a continuous extension of c_t measured in tetragonal phase region. So, the special invariance condition represented by Eq. (1.5) has been well preserved in ferroelectric PMN-PT, which implies the monoclinic phase should be an adaptive phase formed by tetragonal nanodomains. The general invariance condition, $a_{ad} + b_{ad} = a_t + c_t$, adjusted to be $a_m + c_m = a_t + c_t$, has also been checked with the experimental data in Fig. 1.8 and a good agreement has also been found.

15
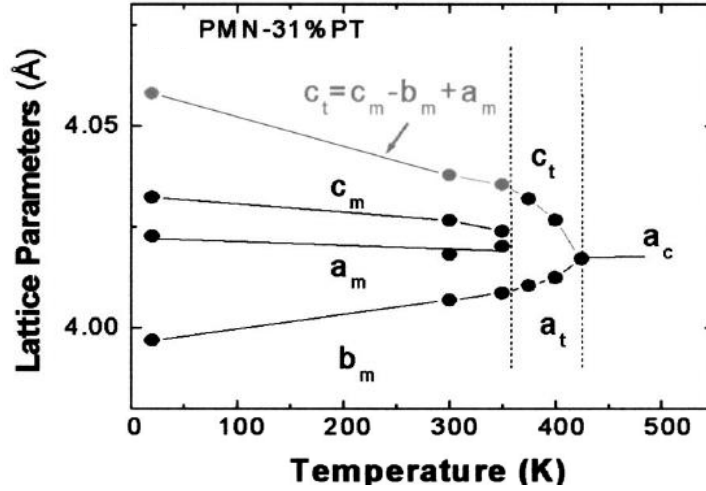
Fig. 1.8 Temperature-dependent lattice parameters of PMN-31%PT [18]. The point and line in gray gives calculated c_t based on Eq. 1.5b. The experimental data points and lines in black are obtained by neutron diffraction [24].

The observed intrinsic relationship between the lattice parameters of monoclinic phase and tetragonal phase stabilized in different temperature regions in ferroelectric PMN-PT strongly supports that the monoclinic phase near MPB is actually an adaptive phase composed of tetragonal nanodomains. It has also been reported [25] that a monoclinic adaptive phase can also be formed by rhombohedral nanodomains. Correspondingly, there is also an intrinsic relationship shown to exist between the lattice parameters of the monoclinic adaptive phase and the rhombohedral phase, which was confirmed as well in PMN-PT system [25].

Fig. 1.9 gives the lattice parameters as function of composition in PMN-PT with rhombohedral, monoclinic and tetragonal phases stabilizing in different composition regions [24]. As Fig. 1.9 shows, for the monoclinic phase observed in the intermediate region where MPB is located, one of its lattice parameters a_m is a continuous extension of a_r (the lattice parameter of rhombohedral) from the

16

rhombohedral phase region near PMN side of MPB, while another lattice parameter b_m is a continuous extension of a_t (the lattice parameter of the tetragonal phase) from tetragonal phase region near PT side of MPB. This intrinsic lattice parameter relationship is also supportive to the adaptive phase model, suggesting that the monoclinic phase at MPB is an adaptive phase acting as a structural bridge connecting the tetragonal and rhombohedral phase.
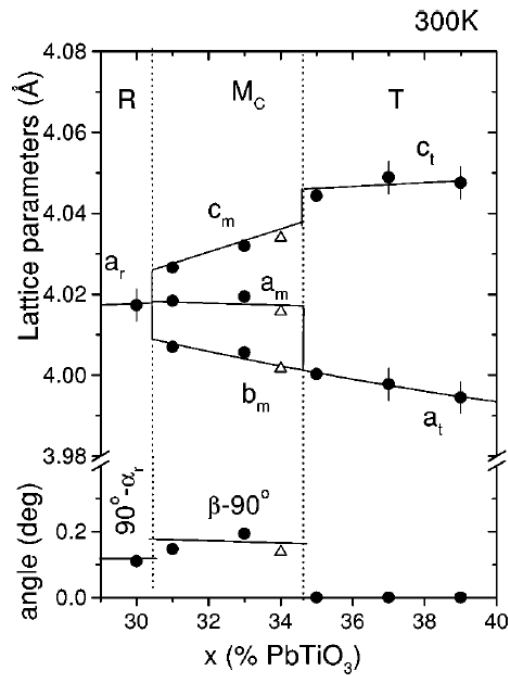
Fig. 1.9 Composition dependence of lattice parameters for rhombohedral, monoclinic and tetragonal phases stabilizing in three different composition regions of PMN-PT [24].

Based on adaptive phase model, the large piezoelectric coefficient in ferroelectrics near MPB can be easily understood. For a monoclinic adaptive phase consisting of nanodomains of two different orientational and polarization variants, an external field (stress/electric field in ferroelectrics) can change the volume fraction of the variants with the fraction of favorably oriented

17

polarization/strain domains increased and the fraction of unfavorably oriented domains decreased, and cause large shape and polarization change. Because strain and polarization are directly correlated in ferroelectrics, the domain rearrangement can be induced either by stress or electric field and will result in large shape and polarization change simultaneously. Therefore, adaptive phase at MPB will show not only large piezoelectric coefficient, but also reduced elastic moduli (structural softening) and peaked dielectric susceptibility which will be shown to be consistent with experimental results later.

1.3 Lead-free ferroelectric BZT-BCT with MPB

PZT has been dominating piezoelectric applications (transducers, actuators, sensors and so on) during the past 50 years due to their large piezoelectric coefficient near MPB with d_{33} = 500-600 pC/N in high-end PZT [26]. However, the usage of lead-containing materials is facing an increasing restriction due to lead toxicity to our environment and human body. Therefore, there has been a concerted effort to develop lead-free piezoelectric materials to replace lead-based piezoelectrics. Most of the work on lead-free piezoelectric materials, has been done in three systems, which are $K_{0.5}Na_{0.5}NbO_3$ (KNN)-based family [27-29], $Na_{0.5}Bi_{0.5}TiO_3$ (NBT)-based family [30-32] and most recently discovered $BaZr_{0.2}Ti_{0.8}O_3$ (BZT)-$Ba_{0.7}Ca_{0.3}TiO_3$ (BCT) system [33-37]. BZT-BCT system is the most promising lead-free alternative for Pb-based piezoelectric materials because a large piezoelectric coefficient d_{33} on the order of 560-620 pC/N [33] has been achieved, which exceeds the piezoelectric coefficient of all other lead-free system and is comparable to the piezoelectric coefficient obtained in PZT.

BZT-BCT is a pseudo-binary ferroelectric system with MPB existing in the temperature-composition phase diagram as presented Fig. 1.10 [33]. Similar to the phase diagram of PZT, in higher temperature region of the phase diagram, BZT and BCT exist as a complete solid solution with paraelectric cubic structure, while in low temperature region, there is a MPB boundary separating rhombohedral phase (near BZT side) region with polarization directed along <111> and tetragonal phase (near BCT side) region with polarization directed along <100>.
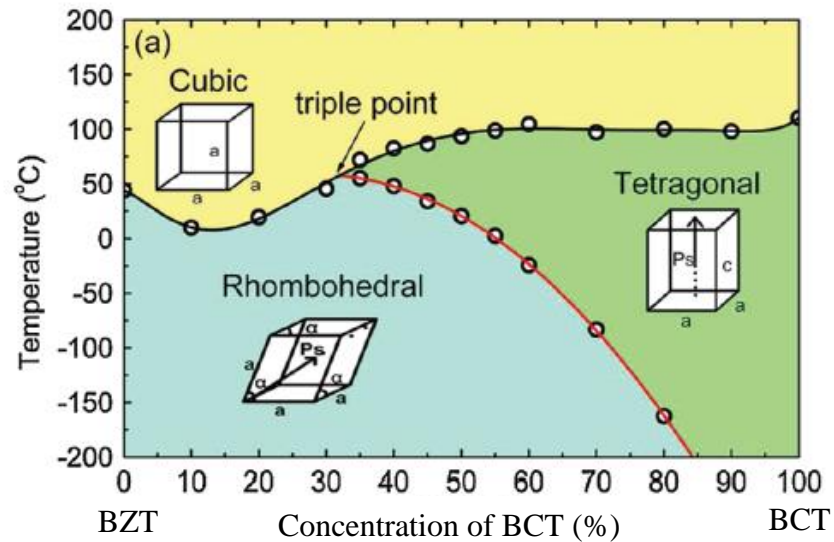
Fig. 1.10 Phase diagram of pseudo-binary system of ferroelectric BZT-BCT with MPB marked as a red line [33].

The piezoelectric coefficient d_{33} of BZT-BCT reaches a maximum at MPB similar to what has been observed in PZT system as given in Fig. 1.11 [33, 35]. It has also been demonstrated in Fig. 1.11 that a series of other electrical and elastic parameters, like dielectric constant ε, saturation and remnant polarization P_m, P_r, and elastic stiffness c_{33}, display a local maximum or minimum at MPB in BZT-

19

BCT. All these behaviors can be perfectly explained if we assume that the adaptive phase at MPB in PZT also forms in this BZT-BCT system. The adaptive phase model for PZT and other related ferroelectric systems described before has provided a perfect explanation to the enhanced piezoelectric response at MPB and has also predicted large polarization and elastic softening at MPB caused by the microtwinned domain structure which can easily be rearranged by applying a stress or an electric field. It is quite reasonable to expect the same adaptive phase existing at MPB in PZT to appear at MPB in BZT-BCT system considering that the phase diagrams of PZT (Fig. 1.1) and BZT-BCT (Fig. 1.10) are highly similar and thus the conditions leading to the formation of an adaptive phase consisting of twin-relate lamellar nanodomains in PZT will probably also be fulfilled in BZT-BCT system.
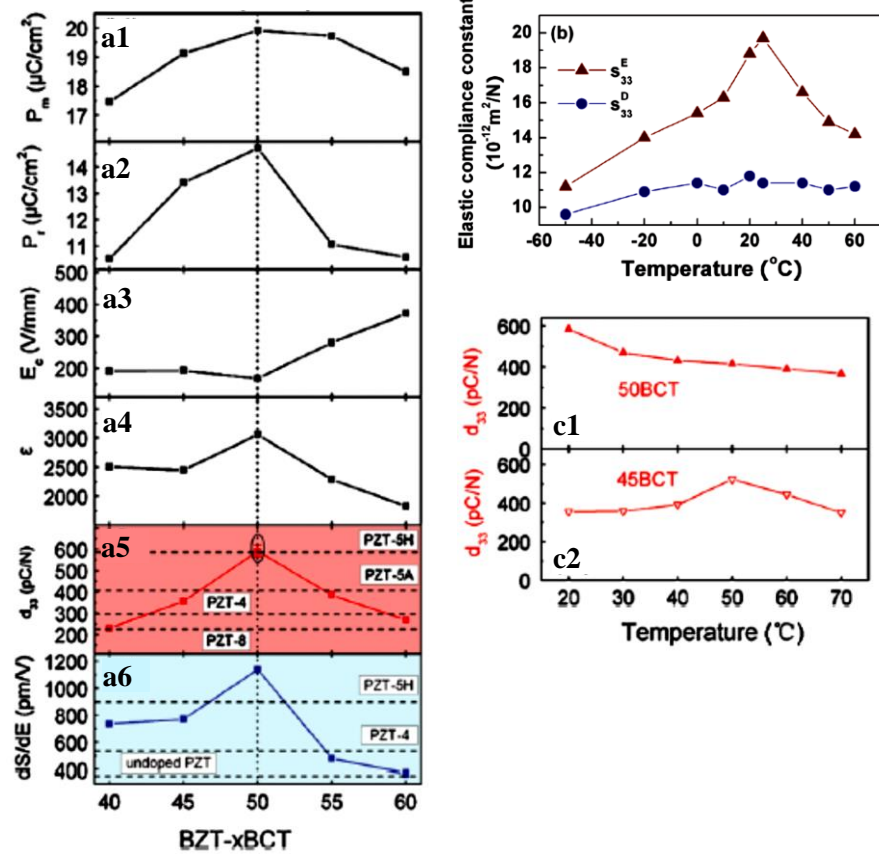
Fig. 1.11 Composition dependences at RT in (1-x) BZT-x BCT [30] of (a1) saturation polarization P_m, (a2) remnant polarization P_r, (a3) coercive field E_c, (a4) dielectric constant, (a5) piezoelectric coefficient d_{33}, and converse piezoelectric coefficient dS/dE. Temperature dependences of (b) elastic compliance constant S_{33} for composition of x=0.5 [35], and (c) piezoelectric coefficient d_{33} for composition of x=0.45 and 0.5 in (1-x) BZT-x BCT system [33].

The microstructures of BZT-BCT have been examined with TEM by Ren and his coworkers [38], and miniaturized nanodomains were observed with MPB approached by varying composition or temperature. Fig. 1.12 displays the evolution of microstructure of (1-x)BZT-xBCT at RT with x changing from 0.4 to 0.6. At x=0.4, a typical rhombohedral domain structure was observed, and the convergent beam electron diffraction (CBED) pattern indicates the existence of a (110) mirror plane, a symmetry element possessed by the rhombohedral phase of R3m near BZT side in BZT-BCT. Correspondingly, at x=0.6, a tetragonal domain

21

structure was found with (001) mirror plane (the symmetry element in tetragonal phase of P4mm near BCT side) identified in the CBED pattern. Interestingly, a domain hierarchy was observed with miniaturized lamellar nanodomain structure emerging within each of the larger-scale plate domain for the MPB composition of x = 0.5. Two sets of CBED pattern have been obtained from the miniaturized lamellar nanodomains, with one of the two sets indicating (110) mirror plane and the other indicating (001) mirror plane. Therefore, we can see from TEM observation that at the MPB of BZT-BCT, the rhombohedral and tetragonal phases coexist in lamellar nanodomains. The temperature dependence of microstructure has also been investigated by TEM for x=0.5 [38], and an evolution similar to what was seen with changing composition has been found as shown in Fig. 1.13. At 60°C, a micro-sized tetragonal domain structure was observed. When the temperature was cooled to 25°C which is the MPB region for x=0.5, a miniaturized nanodomain structure was developed within the tetragonal microdomains. On further cooling to -180°C, a rhombohedral microdomain structure appeared replacing the domain structure at MPB. According to the microstructure evolution with temperature cooling from tetragonal phase region to MPB region, and ultimately to rhombohedral region, it is believed that rhombohedral phase forms within tetragonal domains during the phase transition at MPB and thus leads to the coexistence state of these two phases.
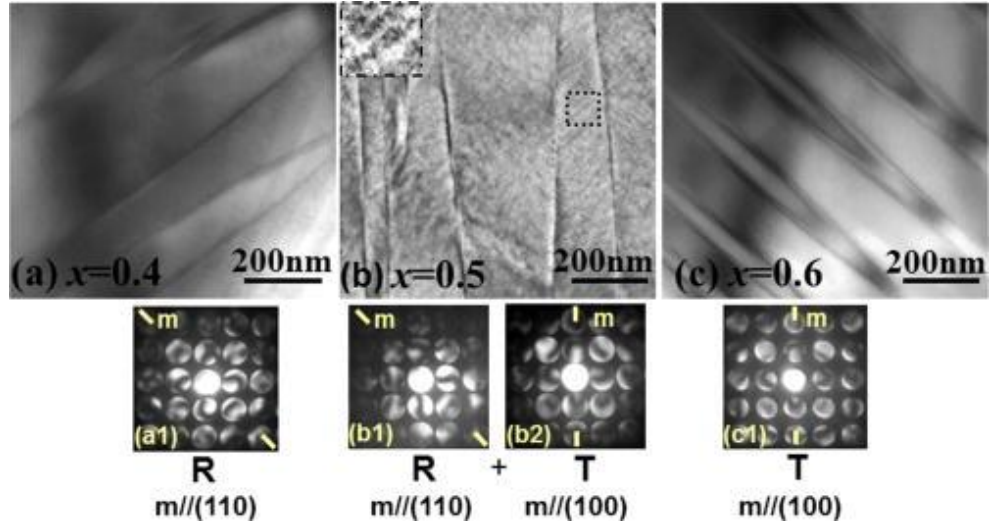
Fig. 1.12 TEM observation on microstructure evolution during composition-induced R-MPB-T transition in (1-x) BZT-x BCT (T = 25 °C and x = 0.4, 0.5, and 0.6) [38]. The bright field TEM images of BZT-xBCT with incident beam along pseudocubic [001] are for (a) x = 0.4, (b) x = 0.5, and (c) x = 0.6. The CBED patterns are obtained from one lamellar domain selected from (a1) x=0.4, (b1) and (b2) x=0.5, and (c1) x=0.6.
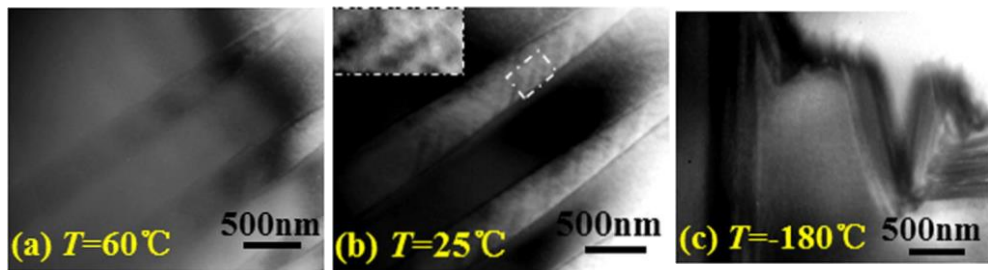
Fig. 1.13 Bright field TEM images at (a) 60°C, (b) 25°C and (c) -180°C for (1-x)BZT-xBCT with x =0.5 [38].

A high-resolution x-ray diffraction study on (1-x)BZT-xBCT was recently reported by Ehmke et al. [39], and the coexistence of rhombohedral and tetragonal phase was identified in a region near MPB which is consistent with the results from the TEM study [38] mentioned above. Fig. 1.14 presents the temperature dependence of synchrotron x-ray diffraction pattern with pseudocubic (200) and (222) reflection covered for BZT-0.45BCT (x=0.45) and BZT-0.5BCT (x=0.5).

Both $(200)_{pc}$ reflection and $(222)_{pc}$ reflection have shown splitting at 25°C for x=0.5 and x=0.45, suggesting the coexistence of both tetragonal phase and rhombohedral phase. However, in x=0.45 composition, the splitting of $(222)_{pc}$ is quite pronounced while the splitting of (200)pc is slight, and the situation is the opposite for x=0.5 composition. Therefore, although both of the two compositions exist as the mixture of two phases, a higher fraction of rhombohedral at x=0.45 and a higher fraction of tetragonal phase at x=0.5 were observed. With increasing temperature, there is more apparent tetragonal splitting and less obvious rhombohedral splitting until rhombohedral splitting disappears and a pure tetragonal phase state is reached at some point after which tetragonal splitting becomes less pronounced and disappears ultimately as a result of the formation of cubic phase.
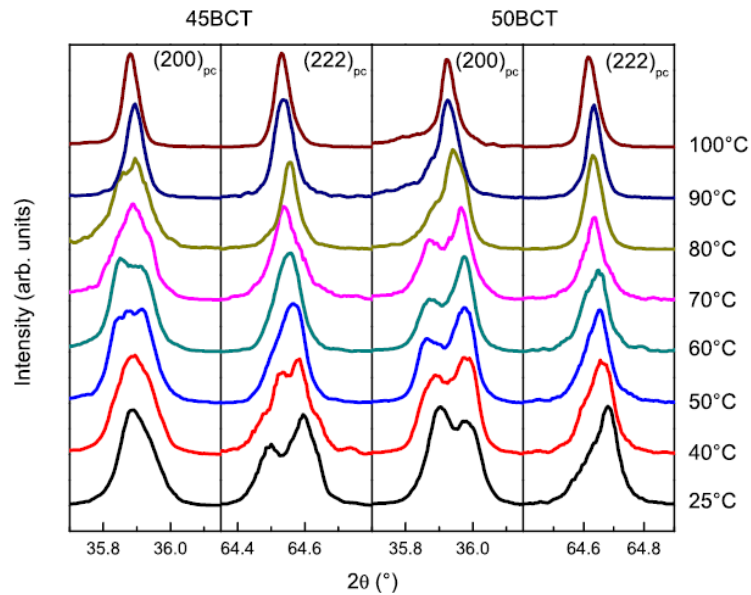
Fig. 1.14 Temperature dependence of in situ synchrotron x-ray diffraction data with $(200)_{pc}$ and $(222)_{pc}$ reflections presented for unpoled (1-x)BZT-xBCT (x=0.4 left, x=0.5 right) [39].

Based on the above structural findings in BZT-BCT, the coexistence of tetragonal and rhombohedral phase with miniaturized nanodomain structure at MPB in BZT-BCT is the structural feature corresponding to the large piezoelectric coefficient and local extremes of other electrical and elastic parameters at MPB. Although the coexistence of tetragonal and rhombohedral phases, instead of monoclinic symmetry observed in PZT and its related systems, has been identified near MPB of BZT-BCT from high resolution x-ray diffraction, the nanotwin structure and property features are perfectly in agreement with what is predicted by the adaptive phase model proposed for PZT and its related systems.

1.4 Motivation:

BZT-BCT has attracted a lot of attention since it's firstly reported to show high piezoelectric coefficient at MPB comparable to that shown by PZT, which makes it a great lead-free candidate to replace PZT used in commercial applications. For applications, BZT-BCT has to be located at MPB where the piezoelectric coefficient is maximized. According to the phase diagram of BZT-BCT (in Fig. 1.10), MPB can be reached by setting an appropriate temperature for any composition in the range covered by the red MPB line. However, the temperature and composition cannot be changed independently. Once the composition is selected, the temperature for this composition to be at MPB is fixed. For example, for the composition BZT-0.5BCT, the piezoelectric coefficient is maximized around room temperature and for room temperature application, this composition will be the best choice. If the position of the MPB can be moved in the phase diagram, then for any operation temperature, there will

be more flexibility in selecting the best composition. It has been reported [40] that doping of Sr into BCT can effectively decrease the Curie temperature of BCT at which cubic-to-tetragonal (paraelectric-to-ferroelectric) phase transition takes place. By reducing the Curie temperature of one of its end members of the pseudobinary phase diagram of BZT-BCT the location of the MPB in this phase diagram can be changed. In this thesis, Sr-doped BZT-BCT ceramics were prepared and their temperature dependence of dielectric properties investigated. In BZT-BCT, the dielectric constant as function of temperature displays peak both at Curie temperature where cubic-to-tetragonal (near BCT side) or cubic-to-rhombohedral (near BZT side) phase transition occurs, and at MPB where tetragonal-to-rhombohedral phase transition occurs, as shown in Fig. 1.15. Therefore, in our work, the Curie temperatures and rhombohedral-to-tetragonal transition temperatures for a series of compositions were determined in Sr-doped BZT-BCT ceramics from their temperature dependence curves of dielectric constant and loss. The dielectric behavior as a function of temperature and composition, and the effect of Sr doping on T_C and the location of MPB in BCT-BZT ceramics were analyzed.
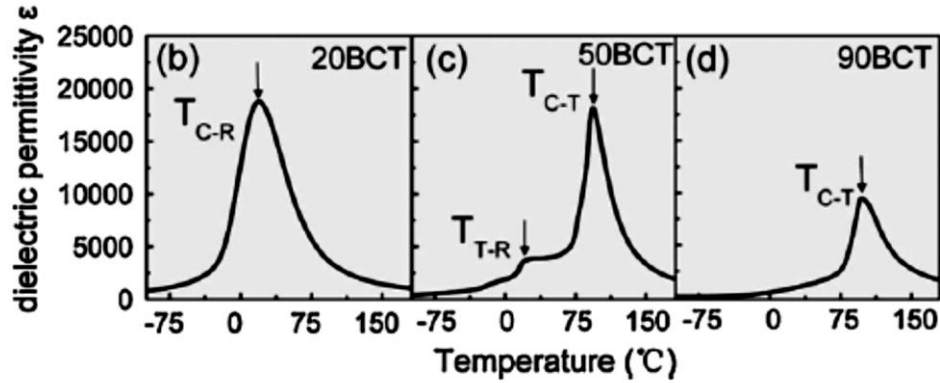
Fig. 1.15 Temperature dependence of dielectric constant for BZT-xBCT ceramics with composition of (a) x=0.2, (b) x=0.5, and (c) x=0.9 [33].

The preparation of BZT-BCT ceramics involves sintering at very high temperature (1450°C-1500°C) if traditional solid-state reaction processing is used, which is not economically favorable. Therefore, it is beneficial to lower the sintering temperature. Sol-gel method is a good choice to achieve this goal since it can produce highly homogenous powders with fine particles. The homogenous powder can allow the synthesis of target phase at lower temperatures because the different elements composing target phase are homogenously distributed in the powder and no long range diffusion distance is required for the elements to react to synthesize the desired homogeneous ceramic. Fine particles are advantageous for promoting densification during sintering and thus can reduce the sintering temperature required to obtain high density ceramics. In our work, sol-gel method has been selected to prepare Sr-doped BZT-BCT powders which are then calcined and sintered at high temperatures to form dense ceramics.

Chapter 2 Sample preparation and characterization

2.1 Sample preparation

A series of ceramic samples of Sr-doped BZT-BCT, with compositions shown in Table 2.1, have been prepared by sol-gel method and high temperature sintering process. The starting materials used are barium acetate (99%), strontium acetate (98%), calcium acetate (99%), zirconium n-propoxide (70% w/w in n-propanol) and titanium n-butoxide (>99%). The preparation procedure has been outlined in the flow chart in Fig. 2.1; First, barium acetate, strontium acetate and calcium acetate were dissolved in acetic acid in a beaker and stirred on a hotplate at 80^oC for 30 minutes, while zirconium n-propoxide and titanium n-butoxide were dissolved in 2-methoxyethanol in a beaker and stirred on hotplate at 80^oC for 30 minutes. Then, acetic acid and 2-methoxyethanol solutions were mixed and continuously stirred on the hotplate at 80^oC for several hours until a viscous gel was formed. After that, the gel was dried overnight in an oven at 90^oC to obtain powder. The powder was subsequently calcined in a tube furnace (Lindberg Blue M, Model STF55433C-1)) at 1000^oC for 3 hours to form crystallized BZT-BSCT oxide powders. The calcined powder was ground with polyvinyl-alcohol (PVA) added as bonding agent before being compacted into pellets (8mm in diameter and ~2mm in thickness) by a press (Model 3851-0, Carver Inc) at a pressure of 100MPa. Finally, the pellets were sintered in a tube furnace for 4 hours at temperatures ranging from 1325^oC to 1375^oC to form ceramic samples.

Table 2.1 Compositions of Sr-doped BZT-BCT ceramics prepared.

		(1-x) BZT
x $(Ba_{1-y}Sr_y)_{0.77}Ca_{0.23}TiO_3$ (BSCT)	y=0.2	x=0.1, 0.2, 0.28, 0.3, 0.32, 0.34, 0.36, 0.4, 0.45, 0.5, 0.55, 1
	y=0 y=0.3,	x=1
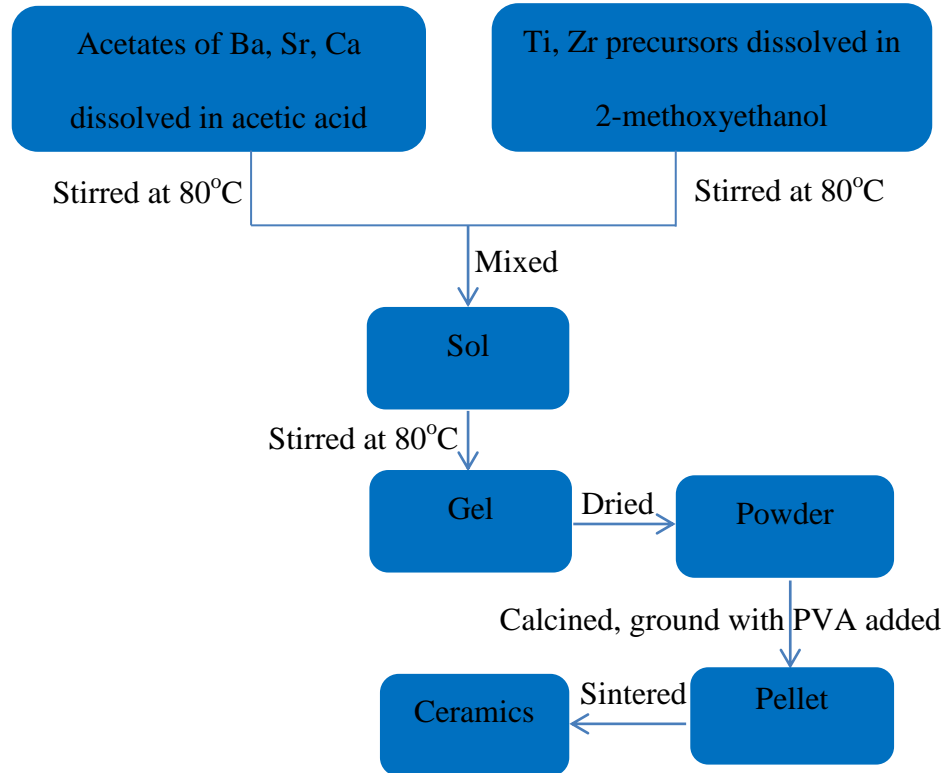
Fig. 2.1 Schematic of the preparation procedures of the BZT-BSCT ceramics.

2.2 Sample characterization

All BZT-BSCT ceramic pellet samples were characterized by Dielectric Analyzer (DEA 2970, TA instruments) through the temperature dependence of dielectric constant and loss measured from room temperature to 240°C at different frequencies (1Hz-10kHz). For this dielectric measurement, the surfaces of all

pellet samples were polished by silicon carbide grinding paper (600 and 1200 grit) before Au was deposited on the two surfaces of each pellet by AJA sputtering unit (AJA international ATC 1800-V) to form electrode layer with thickness of ~500 nm.

The measurement of dielectric constant and loss by DEA is carried out by applying a sinusoidal voltage (produced from a dielectric sensor) to the measured pellet discs and analyzing the current through a dielectric sensor. Fig. 2.2 shows the equipment and the samples' location marked by a red arrow.
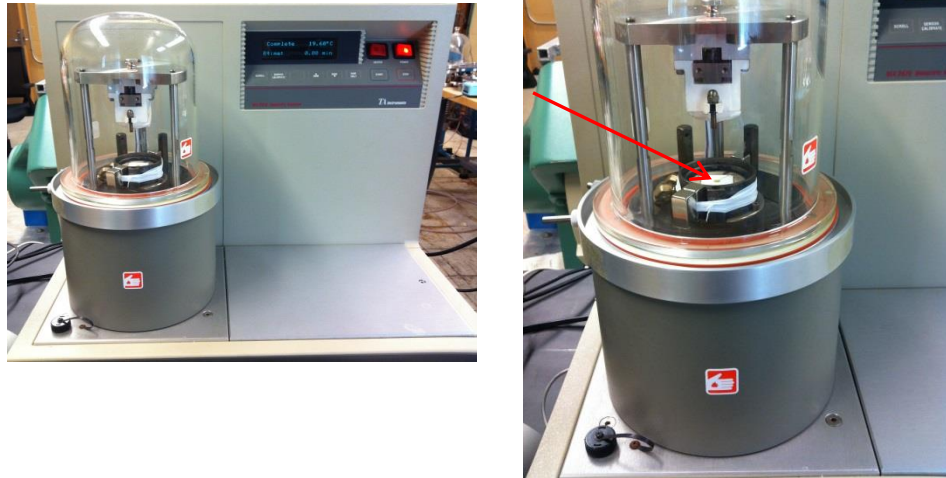
Fig. 2.2 DEA equipment with the stage where the measured samples are mounted, marked by a red arrow.

From the applied voltage and the resultant current, the capacitance (C) of the measured pellets can be obtained. The dielectric constant can then be calculated from the capacitance using

$$C = \varepsilon_r \varepsilon_0 \frac{A}{d}, \tag{2.1}$$

where ε_r is the dielectric constant (or relative permittivity), ε_0 is the vacuum permittivity, A is the area of the measured sample surface covered by electrode, and d is the thickness of the measured sample.

To understand how the capacitance can be obtained from the applied voltage and current, some fundamentals on dielectric materials have to been introduced. A real dielectric material is usually seen to show both characters of a capacitor and a resistor. As a capacitor, a dielectric material can store electrical energy through alignment of dipoles and the resulted gathering of restricted charges on the surface of the dielectric material. In an ideal capacitor, the phases of the voltage and current are different, with the phase of the latter $\pi/2$ ahead of the former. The capacitance C is defined as:

$$C = \frac{q}{V} \tag{2.2}$$

where q is the total charge gathered on the surface of the capacitor, V is the voltage applied. Assume the sinusoidal voltage and current for a capacitor is expressed as $I(t)=I_0\sin(t+\pi/2)$ and $V(t)=V_0\sin\omega t$ with ω being the frequency, t being the time, V_0 and I_0 denoting the amplitude of the sinusoidal voltage and current. Then, C can be calculated as:

$$C = \frac{I(t)dt}{dV(t)} = \frac{I_0 \sin\left(\omega t+\frac{\pi}{2}\right)dt}{dV_0 \sin\omega t} = \frac{I_0}{\omega V_0} \tag{2.3}$$

Eq. (2.3) is only valid for an ideal capacitor. In real dielectric materials, there is always conductivity existing from some free charges which produce current whose phase is consistent with the phase of the voltage. This conductivity character makes the dielectric materials work like a resistor and causes electrical energy dissipation due to resistive heating in a resistor. Therefore, in a dielectric material, with a sinusoidal voltage ($V_0 \sin\omega t$) applied, the phase of the resultant current will be somewhere between 0 and $\pi/2$. The sinusoidal current and voltage can be described as vectors (shown in Fig. 2.3) with size of the vector being the amplitude and the angle θ between the current and applied voltage being the phase difference. The current I can be decomposed into two components, one of which is along the voltage vector V (denoted as I'' in Fig. 2.3), and the other is along the direction perpendicular to V (denoted as I' in Fig. 2.3). I' is the current component with a phase $\pi/2$ ahead of V, while I'' is the current component with the same phase as V. According to Eq. 2.3, the ratio of the amplitude of I' over the amplitude of V is equal to ωC, which is usually called the imaginary part of admittance. The ratio of the amplitude of I'' over the amplitude of V corresponds to conductance or the inverse of resistance, which is usually called the real part of admittance. The ratio of the real part of the admittance over the imaginary part is defined to be dielectric loss which is equal to $\tan\delta$ with the angle δ being $\pi/2-\theta$.

Based on the description above, the amplitude attenuation and phase shift of the current signal compared to the applied voltage yield the dielectric constant and loss.

32
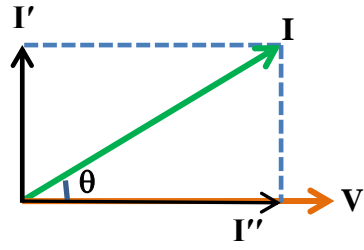
Fig. 2.3 The vector relationship between the applied voltage (V) and resultant current (I) in a dielectric material.

Chapter 3 Results and discussion

BSCT and BSCT-BZT ceramics with compositions listed in Table 2.1 have been obtained by sol-gel method and solid state sintering process with the sintering temperature ranging from 1325^oC to 1375^oC which is $\sim 125^oC$ lower than the sintering temperature used for preparing BCT-BZT ceramics by conventional solid state sintering process which is 1450^oC-1500^oC [33]. Temperature dependences of dielectric constant and loss at different frequencies ($1Hz \leq f \leq 10kHz$) for all compositions have been characterized from RT to 240^oC by DEA, and the results have been presented and discussed.

3.1 Effect of Sr doping on the phase transition in BCT

Fig. 3.1 gives the dielectric constant as function of temperature at 1kHz for pure BCT and Sr-doped BCT ceramics. The dielectric constant ε displays a peak ($\varepsilon_{max} \sim 6800$) at $T_C \sim 135^oC$ for pure BCT which corresponds to the phase transition between paraelectric cubic phase above T_C and ferroelectric tetragonal phase below T_C. For BSCT with 20% Ba replaced by Sr, the dielectric constant peak moves to significantly lower temperature ($\sim 64^oC$) accompanied by higher ε_{max} (~ 9300). When the doping amount of Sr increases to 30%, the dielectric constant peaks at further lower temperature ($\sim 33^oC$) while ε_{max} decreases to ~ 6200. The lower T_C caused by Sr doping can be easily understood since $SrTiO_3$ is stabilized as cubic paraelectric phase at all temperatures without cubic-to-lower symmetry phase transition taking place down to 0 K [41] and thus with Sr doped into BCT, the cubic phase is increasingly stabilized and cubic-to-tetragonal phase transition is delayed to occur at lower temperature.
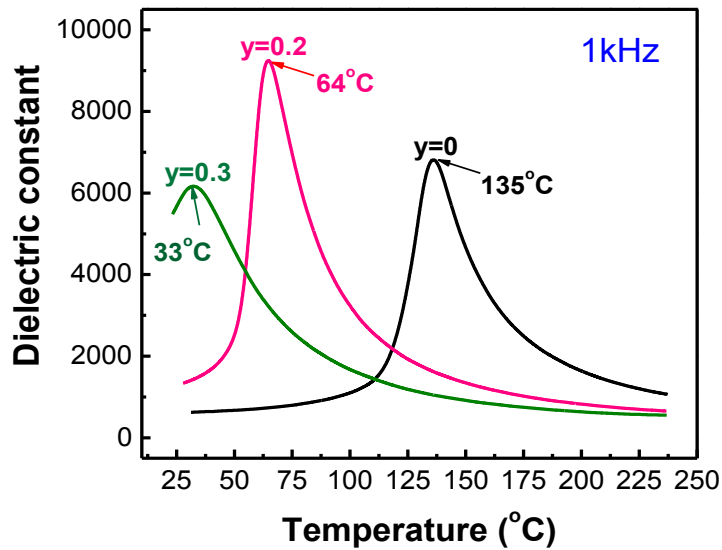
Fig. 3.1 Temperature dependence of dielectric constant at 1kHz for pure BCT and Sr-doped BCT ceramics with y representing the fraction of Ba substituted by Sr.

3.2 Dielectric behavior of xBSCT- (1-x)BZT

BSCT with 20% Ba replaced by Sr were selected to form pseudo-binary system with BZT and the temperature dependence of dielectric constant and loss for different compositions are presented in Fig. 3.2, 3.3 and 3.5.

3.2.1 Dielectric behavior of BSCT-BZT (x= 0.1 and 0.2) in BZT-rich region

Fig. 3.2 shows the dielectric behavior for composition x=0.2 (0.2BSCT-BZT) which is located in the BZT-rich region of the phase diagram of BZT-BCT presented as Fig. 1.10. just as the phase diagram predicts, 0.2BSCT-BZT undergoes one phase transition at $T_C \sim 34.5^{\circ}C$ within the whole temperature range covered in our measurement, in which with decreasing temperature a paraelectric cubic phase changes to a ferroelectric rhombohedral phase accompanied by the

peaked dielectric constant. The paraelectric-ferroelectric transition temperature T_C increases slightly with increasing frequencies, which is called frequency dispersion behavior typical of a ferroelectric relaxor. The temperature dependent dielectric behavior for x=0.1 (shown in Appendix Fig. a-1) is similar to that for x=0.2 except that T_C for x=0.1 is lower (~20°C) and located around the lower limit of the temperature range covered by this study.
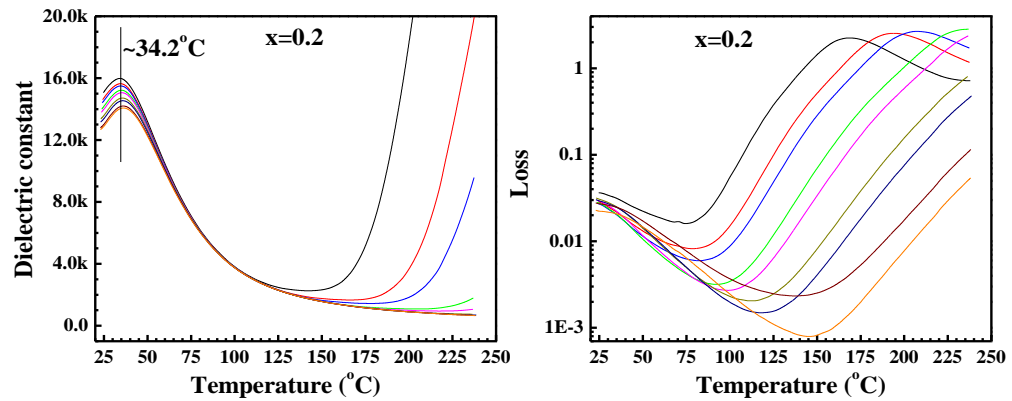
Fig. 3.2 Temperature dependence of dielectric constant (left) and loss (right) at different frequencies in the range of 1Hz ≤f≤10kHz for 0.2BSCT-BZT ceramic.

3.2.2 Dielectric behavior of BSCT-BZT with compositions of 0.28≤x≤0.4

The dielectric behavior as function of temperature for composition x=0.28, 0.3, 0.32 and 0.36 has been displayed in Fig. 3.3. As seen from Fig. 3.3, all four compositions display one dielectric constant peak in the measurement temperature range. The transition temperature T_C increases monotonously with increasing content of BSCT if the anomaly composition x=0.3 is not considered, in which T_C decreases somewhat when compared with x=0.28. The maximum dielectric constants (ε_{max}) at T_C for these four compositions are all larger than ε_{max} shown in

36

0.2BSCT-BZT. Besides, there is also a dielectric loss peak observed for all four compositions at temperatures a little lower than the correspondent T_C where dielectric constant peaks.
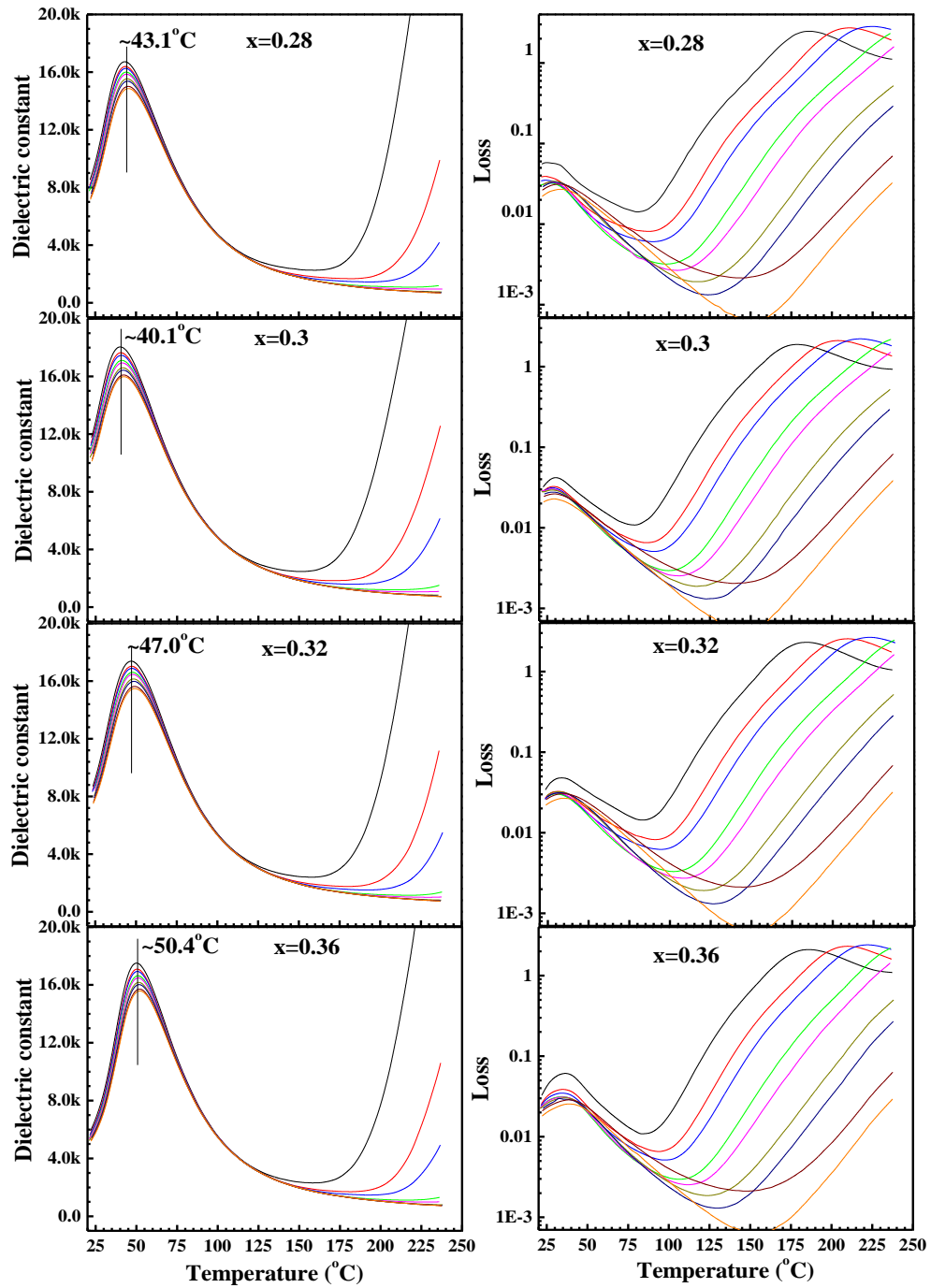
Fig. 3.3 Temperature dependence of dielectric constant, left panels, and loss, right panels, at different frequencies in the range of 1Hz≤f≤10kHz for 0.28BSCT-BZT, 0.3BSCT-BZT, 0.32BSCT-BZT and 0.36BSCT-BZT ceramics.

According to the phase diagram of BCT-BZT, a triple point exists (as shown in Fig. 1.10) where the MPB intersects with the boundary between cubic paraelectric phase and ferroelectric (tetragonal/rhombohedral) phase. If a vertical line is drawn from the triple point until it hits the composition axis on the BCT-BZT phase diagram, a critical composition (x_c~0.32 for BCT-BZT system) can be identified. For compositions of $x \leq x_c$, one phase transition from cubic to rhombohedral phase occurs when the temperature changes in the temperature range covered in the phase diagram. For $x > x_c$, with temperature changes within the phase diagram covered range, two phase transitions can take place, one of which is from cubic to tetragonal phase and the other from tetragonal to rhombohedral phase through MPB. If x is larger than but close to x_c, the temperatures for cubic-to-tetragonal and tetragonal-to-rhombohedral phase transitions are very close to each other and thus might not be distinguishable from the two overlapping dielectric constant peaks in the ε-T curves.

In the BSCT-BZT system, due to doping of Sr, x_c might deviate a little from 0.32, the critical composition of BCT-BZT system. Theoretically, x_c can be roughly estimated by observing the appearance of two dielectric constant peaks in ε-T curves with increasing x. However, as mentioned previously, the two dielectric constant peaks are overlapping and can't be distinguished when x is larger than but close to x_c. Therefore, we have to find another way to identify x_c. From the dielectric behavior of BSCT-BZT with x=0.2-0.4 (dielectric constant and loss as function of temperature for x=0.34 and 0.4 are shown in Appendix Figs. a-2 and a-3), it has been observed that the paraelectric-ferroelectric

39

transition temperature T_C increases continuously with increasing x except that T_C decreases when x changes from 0.28 to 0.3. Therefore, 0.3BSCT-BZT seems to be a special composition. Actually, besides its anomalous T_C, 0.3BSCT-BZT also exhibits the largest peak dielectric constant ε_{max} in all compositions as Fig. 3.4 shows. It has been reported that ε_{max} at T_C should become higher as x approaches x_c and reaches the local maximum for $x = x_c$ in which the corresponding paraelectric-ferroelectric phase transition happens to be at the triple point where the MPB starts and the polar anisotropy disappears [33]. As mentioned before in the introduction of this thesis, the vanishing polar anisotropy at MPB has also been predicted in PZT based on the simplest 2-4-6 free energy approximation of the Ginzburg-Landau-Devonshire theory [10]. Therefore, in all compositions, x=0.3 should be the closest composition to x_c since it gives the largest ε_{max}. The fact that compared to 0.28BCT-BZT, 0.3BSCT-BZT shows decreased T_C, can be attributed to the overlapping of dielectric constant peak at T_C to another peak at lower temperature due to ferroelectric-ferroelectric (tetragonal-to-rhombohedral) transition through MPB.
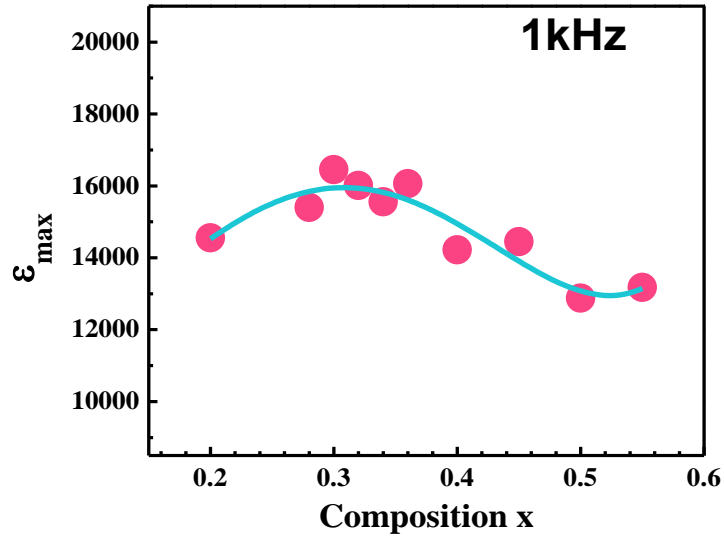
Fig. 3.4 Peak dielectric constant at T_C for 1kHz as function of composition x in xBSCT- (1-x)BZT ceramics.

Based on the discussion above, 0.3BSCT-BZT is already located in the phase diagram region where two phase transitions, cubic-to-tetragonal and tetragonal-to-rhombohedral transitions, can happen with varying temperature. Therefore, although only one dielectric constant peak has been observed in BSCT-BZT ceramics with compositions of x=0.32-0.4 like the case for x=0.3, there are actually two phase transitions happening at very close temperatures and the resulting overlapping of two dielectric constant peaks causes the observation of one peak. In order to be able to see two dielectric constant peaks, the composition has to move further toward BSCT side so that the temperatures for cubic-to-tetragonal and tetragonal-to-rhombohedral transitions will be increasingly split.

3.2.3 Dielectric behavior of BSCT-BZT with compositions of 0.45≤x≤0.55

Fig. 3.5 gives the temperature dependence of dielectric constant and loss for 0.45BSCT-BZT, 0.5BSCT-BZT and 0.55BSCT-BZT ceramics. For x=0.45, although there is still only one dielectric constant peak observed from ε-T curves, an apparent broadening happens for the dielectric loss peaks indicating there are actually two partially overlapped peaks existing corresponding to cubic-to-tetragonal and tetragonal-to-rhombohedral transitions. When the content of BSCT is increased to 0.5 and 0.55, there is a shoulder emerging beside the high dielectric constant peak (due to paraelectric-ferroelectric phase transition) and accordingly, in dielectric loss curves, two peaks can be clearly seen. The maximum dielectric constants ε_{max} at T_C for x=0.45, 0.5 and 0.55 are all smaller than ε_{max} shown by BSCT-BZT ceramics with compositions of x=0.28-0.36 in which the paraelectric-ferroelectric transition is close to MPB.
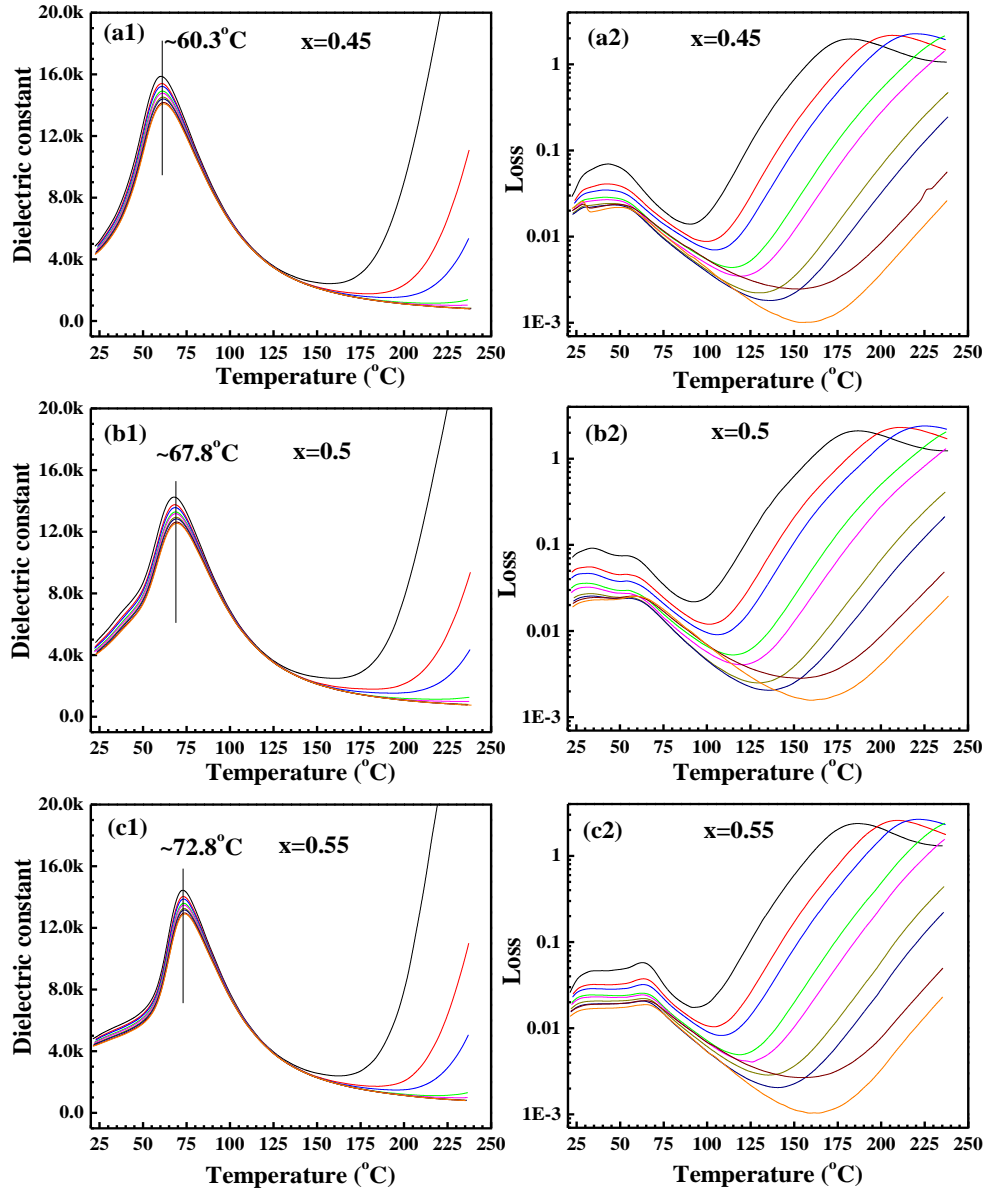
Fig. 3.5 Temperature dependence of dielectric constant, left panels, and loss, right panels, at different frequencies in the range of 1Hz≤f≤10kHz for 0.45BSCT-BZT, 0.5BSCT-BZT and 0.55BSCT-BZT ceramics.

3.2.4 Origin of enhanced ε_{max} (at T_C) for compositions close to x_c and maximized ε at MPB in BSCT-BZT ceramics

The enhanced ε_{max} of BSCT-BZT at compositions (x=0.28-0.36) close to x_c (~0.3) can be attributed to two factors: 1, the polar anisotropy is smaller with

composition approaching x_c where polar anisotropy disappears; 2, with composition getting closer to x_c, T_C is closer to the temperature of tetragonal-to-rhombohedral transition through MPB with vanishing polar anisotropy as suggested by miniaturized domain size at MPB in BCT-BZT system [38]. In BSCT-BZT, for $x < x_c$ (~0.3), with x approaching x_c from BZT side, the decreasing polar anisotropy makes it easier for polarization to rotate between different directions in <111> family and consequently the maximum dielectric constant at T_C increases. Therefore, 0.28BSCT-BZT should display ε_{max} larger than that shown by 0.2BSCT-BZT, which is consistent with the experiment result shown in Fig. 3.4. For $x > x_c$, with x approaching x_c from BSCT side, the enhanced ε_{max} should be related to both decreasing polar anisotropy and closer transition temperature of cubic-to-tetragonal and tetragonal-to-rhombohedral phase transitions. The overlap of two dielectric constant peaks due to close transition temperatures causes larger ε_{max} because two enhancement mechanisms from the two phase transitions are contributing to the dielectric constant.

The dielectric constant shoulder of the dielectric constant peak at T_C observed in BSCT-BZT at x=0.5 and 0.55 indicates that dielectric constant is maximized at MPB where tetragonal-to-rhombohedral transition occurs. The origin of this maximum dielectric constant at MPB is believed to be related to the same mechanism which causes the maximized piezoelectric coefficient at MPB of BCT-BZT system. As described before, coexisting tetragonal and rhombohedral phases and miniaturized nanodomain structure at MPB of BCT-BZT have been experimentally observed by synchrotron x-ray diffraction [39] and TEM [38]. The

miniaturized nanotwinned domain structure is believed to be the evidence and the result of small domain wall energy due to the drastically reduced or vanishing polar anisotropy just as it occurs in PZT and other related lead-based ferroelectric system. Despite the coexistence of tetragonal and rhombohedral phases observed at MPB of BCT-BZT, instead of monoclinic adaptive phase shown at MPB of PZT and other related lead-based ferroelectric systems, there are more properties in common between the lead-free and lead-based systems like their phase diagrams of high resemblance, the maximized piezoelectric coefficient and nanotwinned domain structures at the MPB. Therefore, it is believed that the large piezoelectric coefficient in BCT-BZT and lead-based ferroelectric systems have their origins in the same mechanism in which the nanotwinned structure plays the dominating role just as the adaptive phase theory explains [10, 17-19]. According to the adaptive phase theory, the nanotwinned domains at MPB are both structural and polarization domains, and can be readily rearranged by external fields (stress or electric field) with the growing of favorably oriented domains in the expense of unfavorably oriented domains. As a result, large change in shape and polarization occurs and accordingly the piezoelectric coefficient, dielectric constant and elastic compliance are enhanced at MPB.

3.3 Effect of Sr doping on the phase diagram of xBCT- (1-x)BZT

3.3.1 Effect of Sr doping on T_C in the phase diagram of xBCT-(1-x)BZT

The paraelectric-ferroelectric transition temperatures T_C for all compositions of BSCT-BZT ceramics have been extracted from ε-T curves and

plotted in a temperature-composition phase diagram as shown in Fig. 3.6. All phase transition temperatures for different compositions of BCT-BZT from Ren's work [33] are also presented in Fig. 3.6 as a comparison to show the effect of Sr doping on the phase diagram. As we can see, the paraelectric-ferroelectric transition temperatures T_C of Sr doped BCT-BZT, increases for compositions x<0.28, while T_C decreases for compositions x>0.28. Table 3.1 summarizes the T_C difference ($\Delta T_C = T_{C-BSCT} - T_{C-BCT}$) between different compositions of BSCT-BZT and BCT-BZT. It can be seen from Table 3.1 that $|\Delta T_C|$ ranges from 0.4 to 28°C in the range 0.2≤x≤0.55.
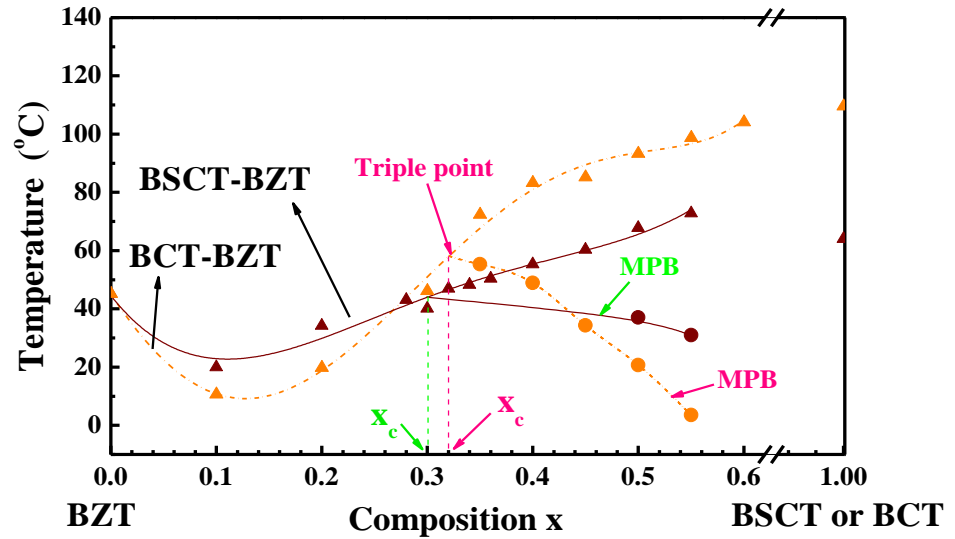
Fig. 3.6 Phase diagram of xBCT-(1-x)BZT and xBSCT-(1-x)BZT systems. The wine triangles, ▲▲▲, are experimental points for BSCT-BZT ceramics studied in this work, and the wine circles, ●●●, are MPB transition temperatures obtained by a fitting and subtraction process carried out on ε-T curves as described in this thesis. Orange triangles, ▲▲▲, and circles, ●●●, are experimental points for BCT-BZT ceramics taken from Ren's work [33].

Table 3.1 The paraelectric-ferroelectric phase transition temperature change (ΔT_C) for different compositions of BSCT-BZT with respect to BCT-BZT.

Composition x	0.2	0.28	0.3	0.32	0.34	0.36	0.4	0.45	0.5	0.55
ΔT_C (°C)	14.4	0.4	-6.1	-11.2	-16.2	-20.4	-28.0	-24.9	-25.5	-26.0

From the phase diagram in Fig. 3.6, it can be found that for the BCT-BZT system T_C decreases first as x increases from 0 to 0.1, then it continues to increase as x increases further from 0.1 to 0.6 and stays almost unchanged for x>0.6, and increases again as x approaches 1. The end member BCT in BCT-BZT system gives the highest T_C in all compositions of x ranging from 0 to 1. For our BSCT-BZT system, T_C also decreases first with T_C of 0.1BSCT-BZT lower than that of BZT, and then starts to continuously increase with x increasing from 0.1 to 0.55. For BSCT-BZT with compositions of x>0.55, T_C continues to increase with x increasing further from 0.55 just like in BCT-BZT system considering the similar trend of T_C change in the range of x=0-0.55 for BSCT-BZT and BCT-BZT systems. However, since T_C of the end member BSCT with x=1 is lower than T_C of compositions of x=0.5 and 0.55, before x reaches 1 there must be a certain composition from which T_C starts to gradually decrease.

To understand T_C change with composition x in BSCT-BZT and BCT-BZT phase diagram, we need to consider how the variation of the fractions of Ba, Sr and Ca in A sites of perovskite ABO_3 and the variation of the fractions of Zr and Ti in B sites can affect T_C. In the phase diagrams of BSCT-BZT and BCT-BZT, at temperatures above T_C, the system forms complete solid solution (both

structurally and compositionally homogenous) and stays in the single phase state in the whole range of x=0-1. Below T_C, the system is compositionally homogenous everywhere with all phase transitions being diffusionless, but is not in single phase state everywhere because the crystal structure varies between different regions. According to high-resolution X-ray study on BCT-BZT [39], near MPB, two phases (structurally distinguished) coexist. Therefore, the analysis on the changes of T_C along the composition axis of the phase diagram is based on the composition change in a compositionally homogenous system.

For xBCT-(1-x)BZT, the chemical formula of this compositionally homogenous system for different composition x can be written as $Ba_{(1-0.3x)}Ca_{0.3x}Zr_{(0.2-0.2x)}Ti_{(0.8+0.2x)}O_3$ which can be seen as Ca and Zr co-doped $BaTiO_3$ with Ca substituting Ba at A sites and Zr substituting Ti at B sites. As x gradually moves from BZT side (x=0) toward BCT side (x=1), the doping fraction of Ca (=0.3x) decreases and the doping fraction of Zr (=0.2-0.2x) increases. The study on $Ba_{(1-x)}Ca_xTiO_3$ [42] found that T_C shows a slight increase with small amounts of Ca doping (less than 8%) and subsequently decreases slightly with continuously increasing Ca doping before reaching the solubility limit (x~0.23-0.3). The doping of Zr in $BaTiO_3$ ($BaZr_xTi_{1-x}O_3$) causes T_C to decrease continuously as the doping fraction x increases from 0 to 0.2 [43]. With the composition x of xBCT-(1-x)BZT gradually increasing from 0 toward 1, the doping fraction of Zr (0.2-0.2x) decreases continuously from 0.2 (x=0) toward 0 (x=1), while the fraction of Ca (0.3x) increases continuously from 0 (x=0) toward 0.3 (x=1). The observed decrease of T_C with changing x from 0 to 0.1 indicates

that at small doping levels the doping of Ca in BZT-rich composition must have played a dominant role in changing T_C and it should have caused decrease of T_C since the decreased Zr fraction should increase T_C for BZT-rich compositions where B-site doping is dominant. With x increasing from 0.1 to 1, T_C of the xBCT-(1-x)BZT system shows initially a continuous increase, then stays almost unchanged for x>0.6, and increases when x is close to 1 demonstrating that T_C change is dominated by decreased fraction of Zr which must have caused an increase of T_C for BCT-rich region since it is known that the increasing doping fraction of Ca slightly decreases T_C for BCT-rich compositions.

For xBSCT-(1-x)BZT system, the changes of T_C along composition axis in the phase diagram can be analyzed in the same way as we did for the BCT-BZT system except that we need to consider the additional effect of Sr doping in A sites. The chemical formula of xBSCT-(1-x)BZT solid solution can be written as $Ba_{1-0.384x}Sr_{0.154x}Ca_{0.23x}Zr_{0.2-0.2x}Ti_{0.8+0.2x}O_3$. With increasing x from 0 to 1, the doping fraction of Sr (0.154x) and Ca (0.23x) increases continuously from 0 (for Ca and Sr with x=0) to 0.154 (for Sr with x=1) and 0.23 (for Ca with x=1), while the doping fraction of Zr (0.2-0.2x) decreases continuously from 0.2 (x=0) to 0 (x=1). According to Yu et al's work [44], doping of Sr in $BaTiO_3$ ($Ba_{1-x}Sr_xTiO_3$) can induce a continuous decrease in T_C as the doping fraction increases from 0 to 1. Sr doping in BCT also causes a continuous decrease in T_C as indicated in Fig. 3 and Cheng's work [40]. As seen from the phase diagram of xBSCT-(1-x)BZT (in Fig. 3.6), with x changing from 0 to 0.1, T_C decreases as it does in BCT-BZT, which indicates that at low doping the co-doping of Ca and Sr in BZT-rich

compositions causes T_C to decrease and this effect overshadows the T_C-increase resulting from decreasing the Zr fraction in the BZT-rich region where B-site doping is dominant. As x increases from 0.1 to 0.55, T_C increases continuously. It is difficult to speculate on the reason because it involves changes in both A-site dopant fraction and B-site dopant fraction in compositions where A-site doping and B-site doping are comparable. Based on our previous analysis on T_C change in the composition range of x =0.55-1, T_C must experience a decrease before x reaches 1 which corresponds to BSCT whose T_C is lower than T_C of compositions with x=0.5 and 0.55. Therefore, in BCT-rich region where A-site doping is dominant, the change of T_C with increasing x is dominated by the increased doping fraction of Ca and Sr which tends to decrease T_C of BCT.

Based on our analysis on the changes of T_C along composition axis in phase diagram of xBSCT-(1-x)BZT, the complete T_C curve as function of x in the whole composition range of 0-1 can be sketched as shown in Fig. 3.7.
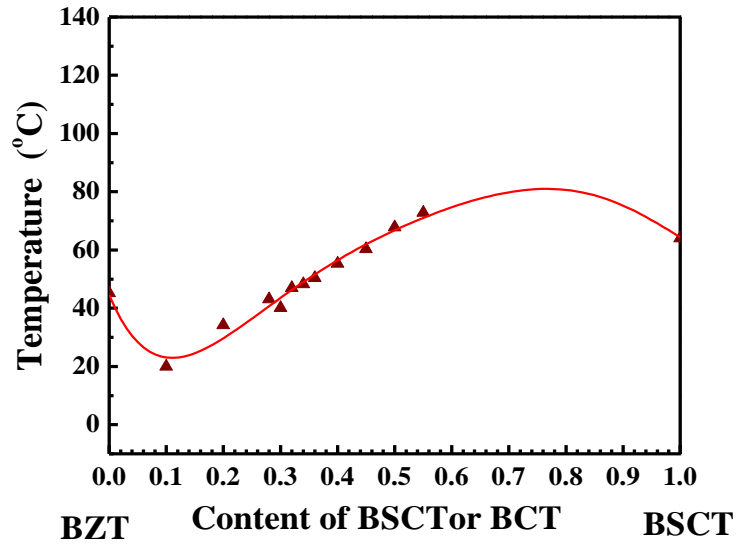
Fig. 3.7 The change of T_C as function of composition x in xBSCT-(1-x)BZT ceramics. The red curve is sketched to approximately describe the continuous change of T_C for x from 0 to 1 based on the experiment data (shown as triangles) (for $0 \leq x \leq 0.55$ and x=1) and empirical prediction (for $0.55 < x < 1$).

3.3.2 Effect of Sr doping on MPB in the phase diagram of xBCT-(1-x)BZT

In order to see how the doping of Sr has affected the MPB location in BCT-BZT phase diagram, the temperature at which the tetragonal-to-rhombohedral phase transition occurs across MPB has to be identified for each composition. However, due to the overlap of the two dielectric constant peaks resulting from cubic-to-tetragonal and tetragonal-to-rhombohedral phase transitions, the temperature of the phase transition across MPB cannot be obtained from ε-T curves for compositions of x=0.3-0.45. However, as discussed previously, the triple point composition x_c for BSCT-BZT is ~0.3, which is different from x_c~0.32 for BCT-BZT. As the starting point of MPB, the triple point has moved in the phase diagram as indicated by the change from 0.32 to 0.3

51

in composition and from 58.0^{o}C to 40.7^{o}C in temperature with Sr doping in BCT-BZT. For x=0.5 and 0.55, the dielectric constant peak of BSCT-BZT for MPB phase transition shows as a shoulder due to partial overlap with the dielectric constant peak caused by the cubic-to-tetragonal transition. However, we will be able to estimate the MPB transition temperature if the dielectric constant peak curve for MPB transition can be extracted from the shoulder in ε-T curve by fitting the dielectric constant peak for cubic-to-tetragonal transition and subtracting the fitted curve from the dielectric constant shoulder. Since there is no available equation built specifically to describe the temperature dependence of dielectric constant in the vicinity of T$_C$, we have used a commonly used peak functions to do the fitting. No satisfying fitting results can be obtained because the dielectric constant peak curve is not symmetric with respect to T$_C$ and no peak function can fit the whole curve for temperatures lower and higher than T$_C$. Since the dielectric constant shoulder for MPB phase transition is on the lower temperature side of the dielectric constant peak curve for cubic-to-tetragonal transition, only this side of the curve is chosen to be fitted by peak functions.

Before fitting the dielectric constant peak caused by paraelectric-ferroelectric phase transition, we need to subtract the background reflecting the high temperature dielectric relaxation (more obvious at lower frequencies) probably caused by electrode-sample boundary effect or oxygen vacancies which are commonly found in ceramics. As shown in Fig. 3.7a, a Gaussian fitting of the dielectric constant curve in the high temperature range at 1Hz for 0.5BSCT-BZT ceramic has produced well fitted curve. Gaussian equation used for the fitting is,

$$y = y_0 + \frac{A}{w\sqrt{\pi/2}} e^{-\frac{2(x-x_c)^2}{w^2}} \tag{3.3-1}$$

Then, the Gaussian fitted curve is subtracted from dielectric constant curve in the temperature range where the dielectric shoulder due to phase transition across MPB and the dielectric constant peak due to paraelectric-ferroelectric transition are located. The subtracted curve is shown in Fig. 3.8b. As this figure demonstrates, the background-subtracted dielectric constant peak at temperatures of $T < T_C$ can be well fitted by Lorentz equation which is expressed as:

$$y = y_0 + \frac{2A}{\pi} \frac{w}{4(x-x_c)^2 + w^2} \tag{3.3-2}$$

After the Lorentz fitted curve was subtracted from the background-subtracted dielectric constant shoulder and a dielectric constant peak was obtained as shown in the set of Fig. 3.8b. As a result, the dielectric peak in the inset of Fig.3.8b yields the temperature of the phase transition across MPB for 0.5BSCT-BZT to be $\sim 37^{\circ}$C. Therefore, with Sr doping, the MPB transition temperature of 0.5BSCT-BZT is 16.3°C higher than that for 0.5BCT-BZT ceramic which is $\sim 20.7^{\circ}$C [33].

Fig. 3.8 (a) Black dotted curve is the experimental dielectric constant as function of temperature for 0.5BSCT-BZT ceramic; red solid curve represents the Gaussian fitting of the experimental dielectric constant in the temperature range where a high temperature dielectric relaxation occurs. (b) Blue curve corresponds to experimental dielectric constant when subtracting the background dielectric constant from the Gaussian fitted curve in (a); the green curve is obtained from the Lorentz fitting of the paraelectric-ferroelectric transition induced peak part of the blue curve with $T<T_C$. The red curve in the inset of (b) is obtained by subtracting Lorentz fitted green curve from the dielectric constant shoulder part of the blue curve. It represents the desired dielectric constant peak due to the phase transition across MPB.

The same fitting and subtraction process has been applied to ε-T curve at 1 Hz for 0.55BSCT-BZT ceramic and the result is presented in Fig. 3.9. From the dielectric peak in the inset of Fig. 3.9b, the MPB phase transition for 0.55BSCT-BZT has been determined to be ~31$^\mathrm{o}$C, which is 27.5$^\mathrm{o}$C higher than the MPB transition temperature (~3.5$^\mathrm{o}$C) of 0.55BCT-BZT [33].
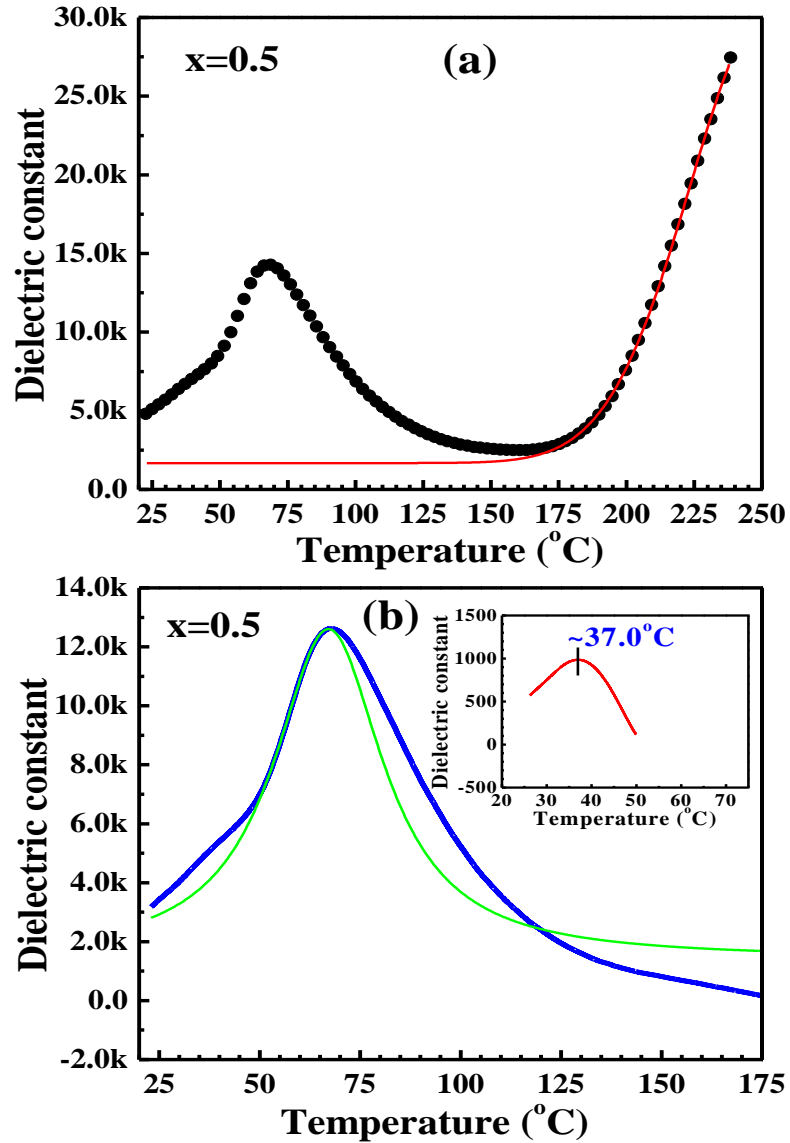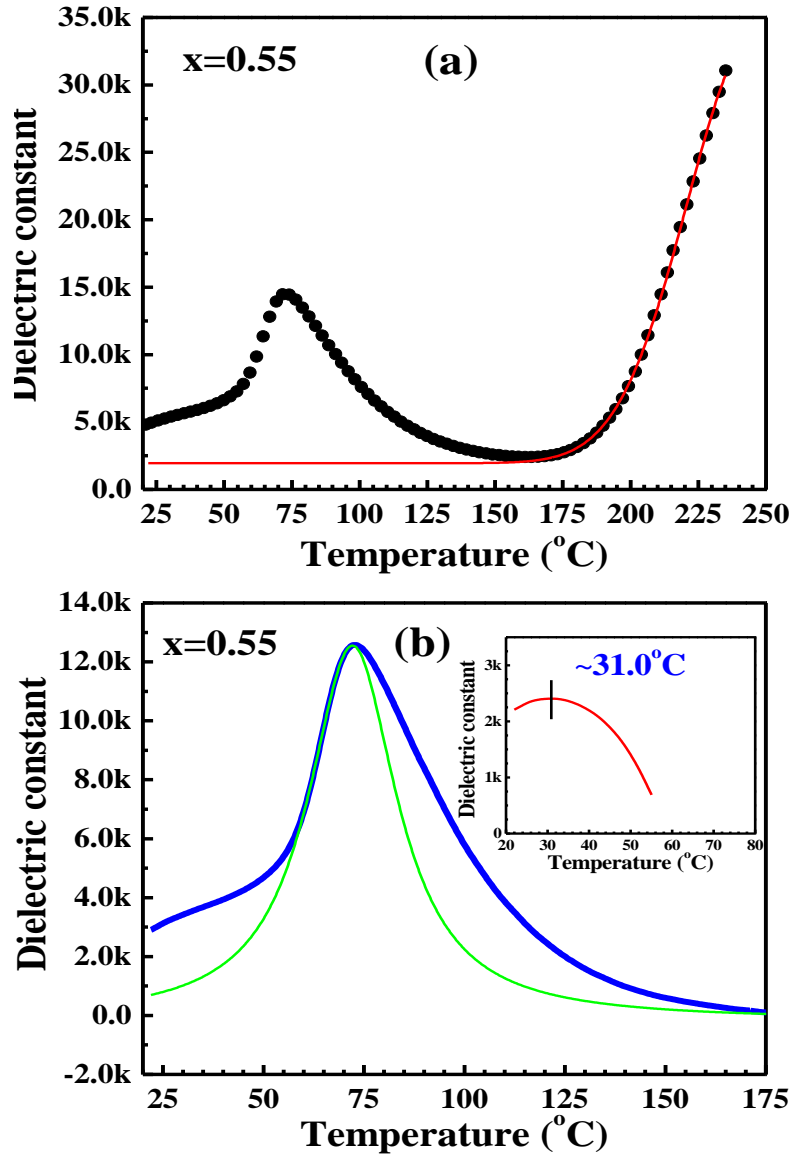
Fig. 3.9 (a) Black dotted curve is the experimental dielectric constant as function of temperature for 0.55BSCT-BZT ceramic; red solid curve represents the Gaussian fitting of the experimental dielectric constant in the temperature range where a high temperature dielectric relaxation occurs. (b) Blue curve corresponds to experimental dielectric constant when subtracting the background dielectric constant from the Gaussian fitted curve in (a); the green curve is obtained from the Lorentz fitting of the paraelectric-ferroelectric transition induced peak part of the blue curve with $T < T_C$. The red curve in the inset of (b) is obtained by subtracting Lorentz fitted green curve from the dielectric constant shoulder part of the blue curve. It represents the desired dielectric constant peak due to the phase transition across MPB.

The MPB transition temperatures for x=0.5 and 0.55 were added into the phase diagram in Fig. 3.6 and thus the MPB boundary of BSCT-BZT has been approximately determined based on the triple point position and MPB transition temperatures for compositions of x=0.5 and 0.55. As we can see from Fig. 3.6, the MPB has been moved by doping of Sr into BCT-BZT with the triple point (the low composition end of MPB) shifting to a point with lower composition and lower temperature and the MPB line being less vertical with respect to composition axis in the phase diagram. Compared with BCT-BZT, the temperature range covered by MPB in BSCT-BZT is closer to room temperature, which is helpful for room temperature application since relevant devices are required to work with piezoelectric coefficient as large as possible which is obtained by approaching MPB as much as possible. In addition, because MPB is less vertical in the phase diagram of BSCT-BZT, the tetragonal-to-rhombohedral transition temperature is less sensitive to composition variation, which is beneficial for practical application because it makes the requirement of precise control on composition less strict. With respect to the flexibility of selecting specific composition for application at a specific temperature, since MPB can be modified by doping, more compositions are available to satisfy the requirement for devices to work at MPB with largest piezoelectric coefficient at the specific operation temperature.

Chapter 4 Conclusion and future work

4.1 Conclusion

BCT, BSCT, and (1-x)BSCT-xBZT ceramics have been obtained by sol-gel method and solid state sintering process. With powders made from sol-gel method, the ceramic sintering temperatures have significantly decreased to $1325^{o}C$-$1375^{o}C$ which are $\sim125^{o}C$ lower than $1450^{o}C$-$1500^{o}C$ used for preparing BCT-BZT ceramics by conventional solid state sintering process. Temperature dependence of dielectric constant and loss for BCT, BSCT and xBSCT-(1-x)BZT (x=0.1-0.55) ceramics have been characterized and analyzed.

Doping of Sr in BCT can significantly reduce the cubic (paraelectric)-to-tetragonal (ferroelectric) phase transition temperature (T_C). T_C is reduced from $135^{o}C$ to $64^{o}C$ with 20% of Ba substituted by Sr in BCT and became $33^{o}C$ with 30% Ba substituted by Sr.

Compared with xBCT-(1-x)BZT, xBSCT-(1-x)BZT, with T_C of the end member BSCT (modified by substituting 20% Ba with Sr in BCT) lower than BCT, shows higher T_C for x=0.1 and 0.2, similar T_C for x=0.28, and lower T_C for x=0.3-0.55. In all compositions studied, x=0.3 has been identified to be the closest composition to the triple point composition (x_c) of BSCT-BZT system based on the two fact that T_C decreases with x increasing from 0.28 to 0.3 while T_C increases with increasing x for all other compositions, and the maximum dielectric constant (ε_{max}) at T_C for x=0.3 is the largest among all compositions. Tetragonal-to-rhombohedral transition temperature for x=0.5 and 0.55 was obtained by subtracting a background calculated by Lorentz and Gaussian fitting

of higher temperature dielectric constant peaks from the lower temperature dielectric constant shoulder in the ε-T dependence.

The phase diagram of pseudo-binary xBSCT-(1-x)BZT system was constructed based on phase transition temperatures for different compositions and was compared with the phase diagram of xBCT-(1-x)BZT. The change of T_C as function of the composition of xBSCT-(1-x)BZT is similar to what is shown in BCT-BZT except that when x is close to 1, with x increasing T_C increases in BCT-BZT system but decreases in BSCT-BZT system. An empirical analysis was made to explain the variation of T_C with compositions for BCT-BZT and BSCT-BZT by considering the existing experimental results on known variations of T_C with doping of Ca and/or Sr in A sites of $BaTiO_3$ and the doping of Zr in B sites of $BaTiO_3$, respectively. Like BCT-BZT, BSCT-BZT also demonstrates the peak dielectric constant (ε_{max}) at T_C which is maximized at the triple point where MPB meets the T_C curve in the phase diagram.

With Sr doped in BCT-BZT, MPB in the phase diagram became more parallel to the composition axis with the triple point shifting to lower composition and lower temperature. The change of MPB location in BCT-BZT phase diagram by Sr doping allows more MPB compositions available for application at a specific temperature with large piezoelectric coefficient required. In addition, the less vertical MPB in the phase diagram of BSCT-BZT is also an advantage because the temperature of tetragonal-to-rhombohedral transition across MPB becomes less sensitive to composition variation, which lowers the requirement of

precise control on composition which is set for the corresponding device to work at/close to MPB so that piezoelectric coefficient is as large as possible.

4.2 Future work

To obtain the complete phase diagram of BSCT-BZT, additional compositions of xBSCT-(1-x)BZT with $0.55 < x < 1$ need to be prepared and their temperature dependences of dielectric constant and loss should be measured to identify their cubic-to-tetragonal transition temperatures (T_C) and the temperatures of tetragonal-to-rhombohedral transition across MPB. A wider temperature range of measurement will be necessary in order to observe the dielectric constant peak in ε-T due to the phase transition across MPB, which will move toward lower temperatures as x increases and thus be out of our current measurement temperature range.

Piezoelectric effect should be investigated to examine how the doping of Sr has affected the piezoelectric coefficient of BCT-BZT, which is scientifically interesting because it can help understand the piezoelectric behavior around MPB in a deeper way and technically helpful in guiding the design of compositions with satisfactory piezoelectric performance for applications.

Appendix: Temperature dependences of dielectric constant and loss for x=0.1, 0.34 and 0.4 of xBSCT-(1-x)BZT ceramics
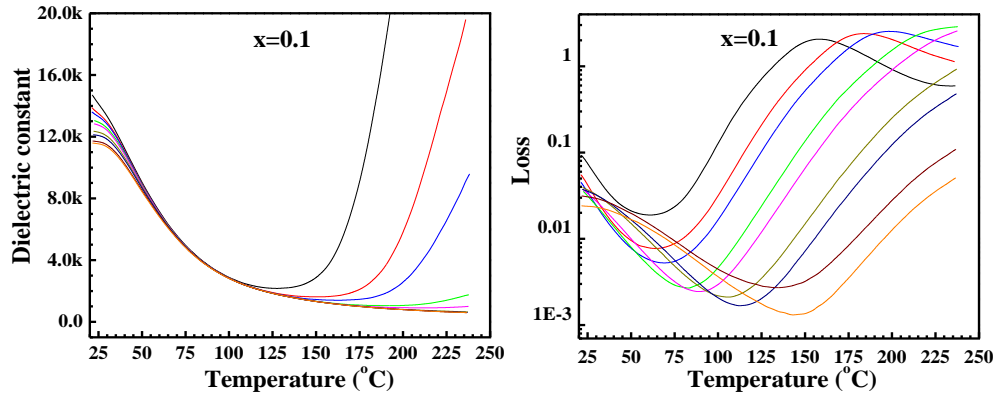

Fig. a-1 Temperature dependence of dielectric constant and loss at different frequencies ranging from 1Hz to 10kHz for 0.1BSCT-BZT ceramic.
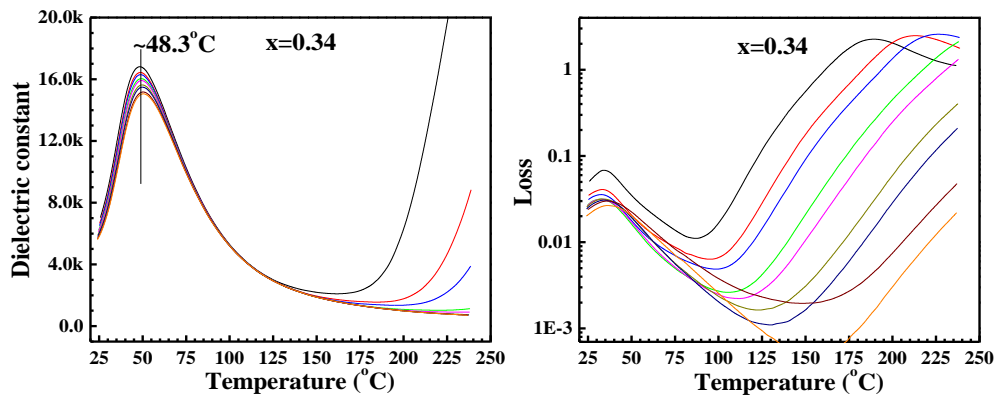

Fig. a-2 Temperature dependence of dielectric constant and loss at different frequencies ranging from 1Hz to 10kHz for 0.34BSCT-BZT ceramic.
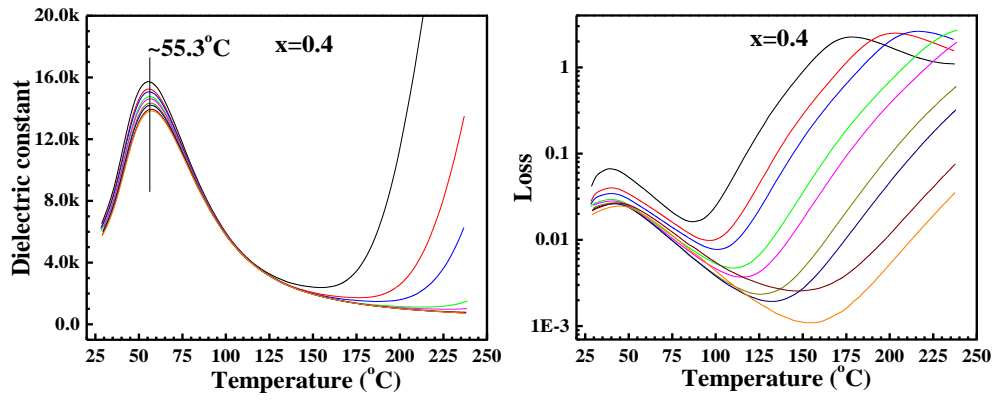
Fig. a-3 Temperature dependence of dielectric constant and loss at different frequencies ranging from 1Hz to 10kHz for 0.4BSCT-BZT ceramic.

Biboliography

1. Yang, S., Bao, H.X., Zhou, C., Wang, Y., Ren, X.B., Matsushita, Y., Katsuya, Y., Tanaka, M., Kobayashi, K., Song, X.P. and Gao, J.R., Phys. Rev. Lett. 104, 197201 (2010).

2. Jaffe, B., Cook, W.R. and Jaffe, H., Piezoelectric Ceramics (Academic Press, New York, 1971) p136.

3. Jaffe, B., Roth, R.S. and Marzullo, S., J. Appl. Phys. 25, 809 (1954).

4. Noheda, B., Cox, D.E., Shirane, G., Gonzalo, J.A., Cross, L. E. and Park, S.-E., Appl. Phys. Lett. 74, 2059 (1999).

5. Noheda, B., Gonzalo, J.A., Cross, L.E., Guo, R., Park, S.-E., Cox, D.E. and Shirane, G., Phys. Rev. B 61, 8687 (2000).

6. Schönau, K.A., Schmitt, L.A., Knapp, M., Fuess, H., Eichel, R.A., Kungl, H. and Hoffmann, M., Phys. Rev. B 75, 184117 (2007).

7. Gorfman, S., Keeble, D.S., Glazer, A.M., Long, X., Xie, Y., Ye, Z.-G., Collins, S. and Thomas, P.A., Phys. Rev. B 84, 020102 (2011).

8. Burkovsky, R.G., Bronwald, Y.A., Filimonov, A.V., Rudskoy, A.I., Chernyshov, D., Bosak, A., Hlinka, J., Long, X., Ye, Z.-G. and Vakhrushev, S.B., Phys. Rev. Lett. 109, 097603 (2012).

9. Fushimi, S. and Ikeda, T., J. Am. Ceram. Soc. 50, 129 (1967).

10. Rossetti, G.A., Khachaturyan, A.G., Akcay, G. and Ni, Y., J. Appl. Phys. 103, 114113 (2008).

11. Xu, G. Luo, H., Xu, H. and Yin, Z., Phys. Rev. B 64, 020102 (2001).

12. Kisi, E.H., Forrester, J.S. and Howard, C.J., J. Phys.: Condens. Matter 15, 3631 (2003).

13. Singh, A.K. and Pandey, D., Phys. Rev. B 67, 064102 (2003).

14. Ohwada, K., Hirota, K., Rehrig, P.W., Fujii, Y. and Shirane, G., Phys. Rev. B 67, 094111 (2003).

15. Noheda, B. and Cox, D.E., Phase Transitions 79, 5 (2006).

16. Guo, R., Cross, L.E., Park, S-E., Noheda, B., Cox, D.E. and Shirane, G., Phys. Rev. Lett. 84, 5423 (2000).

17. Viehland, D., J. Appl. Phys. 88, 4794 (2000).

18. Jin, Y.M., Wang, Y.U., Khachaturyan, A.G., Li, J.F. and Viehland, D., J. Appl. Phys. 94, 3629 (2003).

19. Jin, Y.M., Wang, Y.U. and Khachaturyan, A.G., Phys. Rev. Lett. 91, 197601 (2003).

20. Khachaturyan, A.G., Shapiro, S.M. and Semenovskaya, S., Phys. Rev. B 43, 10832 (1991).

21. Seto, H., Noda, Y. and Yamada, Y., J. Phys. Soc. Jpn. 59, 965 (1990).

22. Schmitt, L.A., Schönau, K.A., Theissmann, R., Fuess, H., Kungl, H. and Hoffman, M.J., J. Appl. Phys. 101, 074107 (2007).

23. Khachaturyan, A.G., Philos. Mag. 90, 37 (2010).

24. Noheda, B., Cox, D.E. and Shirane, G., Phys. Rev. B 66, 054104 (2002).

25. Wang, Y.U., Phys. Rev. B 76, 024108 (2007).

26. Saito, Y., Takao, H., Tani, T., Nonoyama, T., Takatori, K., Homma, T., Nagaya, T. and Nakamura, M., Nature 432, 84 (2004).

27. Guo, Y., Kakimoto, K. and Ohsato, H., Appl. Phys. Lett. 85, 4121 (2004).

28. Hollenstein, E., Davis, M., Damajanovic, D. and Setter, N., Appl. Phys. Lett. 87, 182905 (2005).

29. Matsubara, M., Kikuta, K. and Hirano, S., J. Appl. Phys. 97, 114105 (2005).

30. Takenaka, T., Maruyama, K. and Sakata, K., Jpn. J. Appl. Phys. 30, 2236 (1991).

31. Nagata, H., Yoshida, M., Makiuchi, Y. and Takenaka, T., Jpn. J. Appl. Phys. 42, 7401 (2003).

32. Lin, D., Xiao, D., Zhu, J. and Yu, P., Appl. Phys. Lett. 88, 062901 (2006).

33. Liu, W. and Ren, X., Phys. Rev. Lett. 103, 257602 (2009).

34. Bao, H., Zhou, C., Xue, D., Gao, J. and Ren, X., J. Phys. D: Appl. Phys. 43, 465404 (2010).

35. Xue, D., Zhou, Y., Bao, H., Zhou, C., Gao, J. and Ren, X., J. Appl. Phys. 109, 054110 (2011).

36. Piorra, A., Petraru, A., Kohlstedt, H., Wuttig, M. and Quandt, E., J. Appl. Phys. 109, 104101 (2011).

37. Lin, W., Fan, L., Lin, D., Zheng, Q., Fan, X. and Sun, H., Curr. Appl. Phys. 13, 159 (2013).

38. Gao, J., Xue, D., Wang, Y., Zhang, L., Wu, H., Guo, S., Bao, H., Zhou, C., Liu, W., Hou, S., Xiao, G. and Ren, X., Appl. Phys. Lett. 99, 092901 (2011).

39. Ehmke, M.C., Ehrlich, S.N., Blendell, J.E. and Bowman, K.J., J. Appl. Phys. 111, 124110 (2012).

40. Cheng, X. and Shen, M., Solid State Commun. 141, 587 (2007).

41. Müller, K.A. and Burkard, H., Phys. Rev. B 19, 3593 (1979).

42. Mitsui, T. and Westphal, W.B., Phys. Rev. 124, 1354 (1961).

43. Yu, Z., Guo, R. and Bhalla, A.S., J. Appl. Phys. 88, 410 (2000).

44. Zhang, L., Zhong, W.L., Wang, Y.G. and Zhang, P.L., Solid State Commun. 104, 263 (1997).